Nuclear resonant spectroscopy at Bragg reflections from periodic multilayers: Basic effects and applications

M. A. Andreeva
Department of Physics, M. V. Lomonosov Moscow State University, 119992, Moscow, Russia

B. Lindgren
Department of Physics, Uppsala University, Box 530, 751 21, Uppsala, Sweden
(Received 4 March 2005; revised manuscript received 21 June 2005; published 16 September 2005)

A systematic study of the Bragg nuclear resonant reflectivity from periodic multilayers in the energy and time domains is presented. Using the kinematical approach of the general reflectivity theory we describe the basic features of the time evolution of the reflected wave after a pulsed excitation of resonant multilayers by synchrotron radiation. Effects of the collective excitation have been examined such as the shift of quantum beat phases, the interplay between electronic and nuclear subsystem excitations depending on their relative position in a multilayer, the energy and time evolution of standing waves inside a resonant multilayer, and their influence on the reflectivity spectra. The exact expression for the reflectivity by a thin resonant layer placed inside a multilayer structure has been derived. The observed shift of the delayed reflectivity Bragg peak relative to the prompt peak is explained by the developed formalism. Experimental applications are discussed with examples of magnetic profile determinations in Fe/Cr, Fe/V, and Fe/Co multilayers measured at ESRF.

DOI: 10.1103/PhysRevB.72.125422 PACS number(s): 61.10.Kw, 76.80.+y, 75.70.−i

I. INTRODUCTION

In the last decades great progress has been achieved in fabrication of periodical multilayers with controlled thin-film growth at the atomic level. Such heterogeneous semiconductor, metallic, oxide, and superconducting structures have been investigated intensively. The unique structural, magnetic, electrical, and optical properties, such as perpendicular anisotropy, antiferromagnetic interlayer magnetic coupling, giant magnetoresistance, spin-dependent conductivity, and proximity effects, form the basis of numerous applications of multilayers for new technologies, such as x-ray mirrors, memory cells, spin valves, magnetic recording heads, electro-optical sensors, communication sectors, etc. On the other hand they exhibit an extremely interesting physics of magnetic properties, electronic phenomena, and structural complexity which has not been fully understood yet. There is a lot of evidence that interfaces play a key role in most of the phenomena. Characterization of buried interfaces remains one of the great experimental challenges in material science. For such investigations more and more sophisticated experimental techniques are being developed.[1]

The basic method for multilayer structure investigations has been x-ray or neutron diffraction and grazing-angle specular reflection, but for the understanding of the local magnetic and electronic properties resonant methods such as NMR,[2] Mössbauer or nuclear resonance spectroscopy,[3–5] valence and core-level spectroscopy, and in particular x-ray magnetic circular and linear dichroism as well as spin-polarized photoemission[1] are more informative. Essential improvement of depth selectivity in such investigations up to one atomic monolayer can be achieved with probe-resonant monolayers, e.g., in Mössbauer spectroscopy ^{57}Fe monolayers may be embedded at a definite depth.[3–5] The obvious drawback of such investigations is the necessity to prepare sets of identical samples with different depth positions of the resonant probe layer. Even in the best technological production cycles full reproducibility is difficult to achieve. An alternative is to embed the probe-resonant layer in a step or wedge fashion.[6,7]

Resonant investigations with high depth selectivity can be performed on superstructures when they are combined with specular reflection or diffraction. Mössbauer spectra at total external reflection from a ^{57}Fe mirror were already measured in 1963 by Bernstein and Campbell.[8] Since that time only a few Mössbauer experiments in grazing geometry were performed,[9–17] qualified as "the exotic side of the method."[18] The main difficulty was the low intensity obtainable with radioactive sources when selected within the small angular divergence ($\sim$0.5 mrad) required for reflectivity measurements. This difficulty does not exist for synchrotron radiation (SR) which is naturally strongly collimated. SR beams of high brilliance supply the possibility to investigate the reflectivity with high accuracy on a large angular scale and in the energy range needed for nuclear resonances as well as to perform x-ray resonant spectroscopy near the atomic absorption edges. When beamlines for nuclear resonant scattering had been developed at the third-generation SR facilities (ESRF, APS, KEK, SPRING-8), the nuclear resonant reflectivity at grazing angles ("synchrotron Mössbauer reflectometry") became a standard method for thin-film and multilayer investigation (see, e.g., the review by Chumakov *et al.*[19]).

The essential difference between nuclear resonant spectroscopy with SR and ordinary Mössbauer spectroscopy lies in the energy resolution of the incident radiation. In Mössbauer spectroscopy an "energy scan" of the hyperfine-split nuclear transitions is performed, while supermonochromatization of SR up to the width of the nuclear resonant line ($\sim 10^{-8}$ eV in the case of ^{57}Fe) is extremely difficult. However, the pulsed structure of SR provides the possibility to

investigate the nuclear decay in the time domain and the hyperfine splitting is characterized by quantum beats in the time evolution of the nuclear resonant scattering (see Ref. 20 and references therein). This circumstance leads to specific peculiarities of Mössbauer spectroscopy with SR, which have been discussed in many papers (for a review, see Ref. 21) but here we shall focus our attention on some other effects related to the reflectivity process itself.

Spectroscopy of the reflectivity signal reveals some additional features in reflectivity theory. In particular, the reflectivity is usually considered as the total result of interaction of radiation with the whole multilayer (multibeam interference), but with a spectroscopic analysis it became possible to discuss the different contributions from different groups of atoms or resonant nuclei to the reflectivity signal. For example, the delayed integral reflectivity of the nuclear resonance scattering (delayed due to the finite lifetime of the resonant nuclear level) provides actually a way to select the nuclear resonant response from the prompt electronic scattering. Another feature is the appearance of a peak, near the critical angle for total external reflection, in this delayed integral reflectivity curve,[22,23] different from the ordinary reflectivity curve. Due to the sensitivity of the nuclear resonant scattering to the magnetic alignment, additional Bragg peaks appear on the delayed nuclear resonant reflectivity curve when the magnetic period of the superstructure differs from the chemical one,[22,24,19] similar to what is seen in polarized neutron reflectometry. In this article we shall also discuss the shift of the delayed Bragg peak relative to that observed in the prompt reflectivity curve. Use of the radiation field transformation and the standing-wave concept will turn out to be very efficient for the description of the selected contributions to the reflectivity signal.[25]

Another example of the drawbacks of the ordinary reflectivity theory when combined with the spectroscopic analysis is the description of the influence of roughness. The commonly used Nevot-Croce or Debye-Waller attenuation factors[26,27] do not describe the peculiarities of the influence of roughness on the different spectrum contributions to the reflectivity signal.

Going to the spectroscopy analysis, we should keep in mind that reflectivity spectroscopy differs in many aspects from common transmission spectroscopy. In the first papers on Mössbauer total external reflection[8,9] it was shown that resonant lines in reflectivity spectrum have an asymmetric dispersionlike shape in accordance with the ordinary Fresnel formula with a dip at angles lower than the critical angle and a peak at larger angles (see also the experimental results[16,17]). The line shape becomes even more complicated near a Bragg maximum[12,13,19] for periodic resonant multilayers. Extremely broad and distorted lines were observed in pure nuclear reflections from grazing-incidence antireflection films.[14,28–33] For the conversion electron Mössbauer spectra (CEMS) measured at total reflection, a resonant distortion of the "background line" appears (in addition to the distortion of the resonant lines itself) as a result of the modulation of the photoelectron yield by the resonant dependence of the radiation field inside the resonant media.[34–36] Another complication of the spectrum analysis arises in the time representation of the reflectivity spectrum where dynamical beats, enhancement of the initial decay, and speed-up effects essentially change the simple quantum beat pattern[19,37] (in the same manner as for the saturated forward scattering[21]).

These circumstances make the numerical analysis of the reflectivity spectra more complicated compared to the analysis of absorption spectra but do not invalidate the main subject of the spectroscopic analysis: the relative weights of the contributions. In the reflectivity spectrum, as distinct from the absorption spectra, the relative weights of different contributions strongly depend on the depth position, smoothness of the resonant scattering distribution, and small variations of the angle. The description and explanation of such effects will be the main purpose of the present paper.

A main advantage with reflectivity spectroscopy is the pronounced decrease of the radiation penetration depth (up to $\sim$3 nm) at angles less than the critical angle of the total external reflection ($\sim$3.8 mrad for pure iron and 14.4 keV radiation) with the ensuing increase of the surface sensitivity of the method. Beyond the critical angle the penetration depth is gradually increased, additional spectrum components from deeper layers are added to the reflectivity spectrum, and we obtain the possibility to perform a "depth scan." Impressive experimental examples of investigations of the depth distribution of corrosion products in ^{57}Fe thin films using grazing- incidence Mössbauer spectroscopy (Mössbauer reflectometry in the energy domain) were presented in Refs. 11, 15, 35, and 36 and using the time domain "synchrotron Mössbauer reflectometry" in Refs. 38 and 19.

For the Bragg reflectivity from periodic multilayers this simple idea about penetration depth does not work. However, as we are going to show here, the depth selectivity of the Bragg reflectivity spectroscopy becomes even more essential when it is applied to one repetition period of the multilayer structure. An excellent demonstration of such a structure sensitivity of the resonant x-ray Bragg reflectivity was given by Sève *et al.*[39] where the magnetic moment depth profiles in a repetition period of Ce/Fe and La/Fe structures were obtained from $L_{2,3}$-edge reflectivity spectra.

In general, the analysis of the contributions to the reflectivity spectrum is quite complicated because reflectivity is a coherent sum of waves multiple-reflected by all boundaries in the multilayer. In our discussion of the Bragg reflectivity we shall use the kinematical approximation of the reflectivity theory,[40] being reasonably good for glancing angles much larger than the critical angle of total external reflection. This approximation gives a clear picture of the interference process between reflected waves and even describes the standing-wave influence on the reflectivity[25,41–44] via the generalized Laue function, at least on a qualitative level. When necessary we compare the kinematical approximation with full numerical calculations using the Parratt formalism,[45] or generalized recurrent formalism for anisotropic multilayers.[46,47]

In this paper we present a detailed analysis of the reflectivity spectrum formation and explain different effects appearing in the spectral shape. The normal interference effects have the most pronounced influence on the intensity of the different spectral lines in the energy domain and on the shift of the phases of quantum beats in the time domain. However, the collective character of the multilayer excitation reveals

itself even for systems with relatively small amount of repetitions. The most surprising thing is the time dependence induced into the electronic response which in the absence of resonant nuclei is just prompt. This leads to additional interference contributions in the reflectivity time spectrum and is a true signature of the collective character of the excitation in a resonant multilayer. Other evidence is the existence of an interference peak previously observed in the delayed reflectivity curve,[22,23] being the result of the influence of the electronic response on the nuclear subsystem excitation. Here we will show that analogously it is possible to observe a shift of the delayed Bragg peak relative to the prompt electronic one. The derived formula for the reflectivity of a thin layer placed inside a periodical multilayer explains this results in terms of standing waves. We present a number of model examples which illustrates various peculiarities observable in the reflectivity spectra in both the energy and the time domains and show how these effects may be used in order to extract depth-selective information of the local magnetization. The analyses of experimental nuclear resonant reflectivity data obtained for the periodic multilayers ^{57}Fe/Cr, ^{57}Fe/V, ^{57}Fe/Co, and thin ^{57}Fe films in a nonresonant periodic structure are discussed.

II. THE KINEMATICAL APPROXIMATION

The well-known Parratt recursive algorithm[45] is usually used for calculations of the reflectivity,

$$R_j = \frac{r_j + R_{j+1} e^{2i\varphi_j}}{1 + r_j R_{j+1} e^{2i\varphi_j}}. \tag{1}$$

Here r_j is the Fresnel amplitude of the reflection at the boundary between layer numbers $j-1$ and j. R_{j+1} is the coefficient of the multiple reflection at the previous boundary between the j and $j+1$ layers, $\varphi_j = \kappa \eta_j d_j$ is the phase shift for the reflected wave in layer j having the thickness d_j, and η_j is the projection of the wave vector (in units of $\kappa = 2\pi/\lambda$) on the surface normal $\mathbf{q}$,

$$\eta_j = \sqrt{\sin^2 \vartheta + \chi_j}, \tag{2}$$

where ϑ is the glancing angle of incidence. The indexing is running from the top to the substrate, i.e., $j=0$ is the outer space above the sample surface (air or vacuum) and $j = N+1$ corresponds to the "infinitely thick" substrate on which the N layers are grown. The susceptibility χ_j of layer j is given by

$$\chi_j = \frac{4\pi}{\kappa^2} \rho_j f_j = \frac{\lambda^2}{\pi} \rho_j f_j \tag{3}$$

where f_j is the forward scattering amplitude and ρ_j is the volume density of the scattering centers. For monatomic substances it can be calculated from the density and atomic weights (the important x-ray data are available on the worldwide web[48]). In our case f_j includes the electronic charge scattering as well as the nuclear resonant scattering:

$$f_j = f_j^{\mathrm{el}} + f_j^{\mathrm{nuc}}(\omega). \tag{4}$$

For the electronic part we have

$$f^{\mathrm{el}} = -r_0 (Z + \Delta f' + i \Delta f'') \tag{5}$$

where r_0 is the radius of the electron, $Z + \Delta f'$ and $\Delta f''$ are the real and imaginary parts of the atomic scattering amplitude in units of r_0 (the atomic amplitude of x-ray scattering can be taken from Ref. 49). The nuclear resonance part of the susceptibility is energy (or frequency) dependent:

$$\chi^{\mathrm{nuc}}(\omega) = -\lambda\!\!\!^{-} \mu^{\mathrm{nuc}} \sum_i \frac{A_i \Gamma_i / 2\hbar}{\omega - \omega_i + i\Gamma_i/2\hbar}. \tag{6}$$

If A_i is normalized so that $\Sigma_i A_i \Gamma_i = \Gamma_{\mathrm{nat}}$ (Γ_{nat} is the natural total linewidth of the resonance), then the linear nuclear absorption coefficient μ^{nuc} is

$$\mu^{\mathrm{nuc}} = \sigma_{\mathrm{res}} \rho f^{\mathrm{LM}} P \tag{7}$$

where $\lambda\!\!\!^{-} = \lambda/2\pi = 1/\kappa$,

$$\sigma_{\mathrm{res}} = \frac{2\pi}{k^2} \frac{2I_e + 1}{2I_g + 1} \frac{\Gamma_\gamma}{\Gamma_{\mathrm{nat}}}$$

is the cross section of the nuclear resonant absorption, $I_{e,g}$ are the spins of the exited and ground states, $\Gamma_\gamma / \Gamma_{\mathrm{nat}} = 1/(1+\alpha)$ is the ratio of the radiative linewidth to the total linewidth, α is here the conversion coefficient [for ^{57}Fe, $\sigma_{\mathrm{res}} = 2.56 \times 10^{-4}$ nm^2 (Ref. 50)], ρ is the volume density of resonant nuclei, f^{LM} is the probability of the Mössbauer effect, and P is the enrichment of the nuclear resonant isotope. In the case of α-Fe $\rho = 84.9$ nm^{-3} and we have $\lambda\!\!\!^{-}\mu^{\mathrm{nuc}} = 1.98 \times 10^{-4}$for $f^{\mathrm{LM}} = 0.7$ and $P = 0.95$.

The Parratt formula (1) takes into account the multiple interference of all the waves successively reflected by the boundaries of each layer. It is equivalent to the exact solution of the Maxwell equations for a stratified medium. Such an approach is often called a dynamical theory. Multiple interference presented by Eq. (1) corresponds to a rather complicated picture of interaction so qualitative analysis of the spectrum formation is not feasible on the basis of Eq. (1). However, for Bragg reflectivity investigations at angles essentially larger than the critical angle ϑ_c of the total external reflection of x rays [$\vartheta > (2-3)\vartheta_c$], the kinematical approximation can be effectively used (as was done for the resonant magnetic $L_{2,3}$ x-ray spectrum fit in Ref. 39). Such an approximation can be obtained from the Parratt formula (1) as the result of the following successive simplifications. First we neglect multiple scattering and consequently the denominator in Eq. (1). Second, when $\sin^2 \vartheta \gg \chi$, we can expand Eq. (2) as

$$\eta \approx \sin \vartheta + \frac{\chi}{2 \sin \vartheta}. \tag{8}$$

And third the Fresnel expression for the reflectivity can be replaced by its approximate formula

$$r_j = \frac{\eta_{j-1} - \eta_j}{\eta_{j-1} + \eta_j} \approx \frac{\chi_{j-1} - \chi_j}{4 \sin^2 \vartheta}. \tag{9}$$

Accordingly, the phase difference between waves reflected by two subsequent boundaries j and $j+1$ becomes

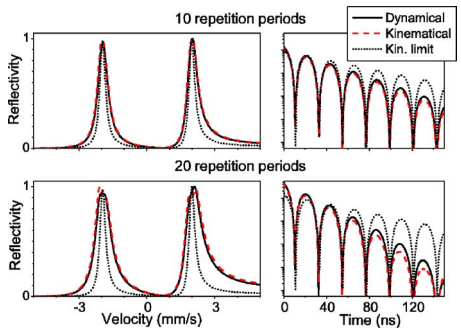

FIG. 1. (Color online) Comparison of the energy and time spectra shape of reflectivity at the Bragg angle, calculated in the dynamical approximation of the reflectivity theory by formula (1) (solid curve), in the general kinematical approximation by formula (11) (dashed curve), and in the simplest kinematical approximation by formula (12) (dotted curve). The model is described in the text.

$$e^{2i\varphi_j} \approx e^{2i\kappa d_j(\sin\vartheta+\chi_j/2\sin\vartheta)}. \tag{10}$$

Hence, we get the following general kinematical formula for the reflectivity amplitude:

$$R = \frac{1}{4\sin^2\vartheta}\sum_{j=1}^{L}(\chi_{j-1}-\chi_j)\exp\left[i\left(Qz_{j-1}+\frac{\kappa}{\sin\vartheta}\sum_{k=1}^{j-1}\chi_k d_k\right)\right], \tag{11}$$

where z_{j-1} is the depth of the boundary between layers $j-1$ and j, calculated from the surface $z_0=0$, and $Q=(4\pi/\lambda)\sin\vartheta$ is the scattering vector. Formula (11) has an obvious interpretation as a sum of waves reflected by all boundaries in the multilayer, accounting for the proper phase difference. In Eq. (11), which in our definition describes the general kinematical approximation, absorption and refraction effects on the phase factors are still taken into account.

The kinematical formula (11) reduces to the simplest form (kinematical limit) if we further neglect the absorption and refraction in the phase shifts of the different contributions:

$$R = \frac{1}{4\sin^2\vartheta}\sum_{j=1}^{L}(\chi_{j-1}-\chi_j)e^{iQz_{j-1}}. \tag{12}$$

In Ref. 40 the different kinematical approaches are compared by calculations of the reflectivity curve as a function of the angle. It was shown that only near the total external reflection angle does the the full Parratt formula have to be used and at the larger glancing angles one may even use the simplest kinematical limit. Here we analyze the applicability of the kinematical approach for the description of the reflectivity spectra in the energy and in the time domain (Fig. 1).

In the calculations we have used a simple model system: a periodic $[^{57}\mathrm{Fe}(1.5\ \mathrm{nm})/\mathrm{V}(1.5\ \mathrm{nm})]_N$ multilayer (N is the number of repetitions) with an *ad hoc* 21 T magnetic hyperfine field on the ^{57}Fe nuclei oriented perpendicular to the layer boundaries (only the second and fifth lines in the sextet spectrum are then excited by the linear σ-polarized SR beam). The enrichment $P=0.5$ was chosen. The exact first-order Bragg angle is 14.75 mrad for a 3 nm repetition period and a resonant wavelength of 0.086 nm. Figure 1 shows that the main features of the spectra are quite similar for all three methods of reflectivity calculation. The general kinematical approximation deviates very little from the exact calculations and even the simplest kinematical approximation reproduces the main features of the spectra rather well for a qualitative analysis. However, the difference of the spectrum shapes increases with the number of repetition periods, so for more accurate calculations (e.g., in a fit procedure) the effects of the multiple scattering (dynamical interaction of radiation with the sample) should be taken into account.

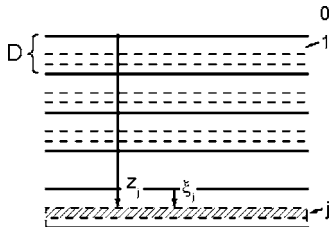

FIG. 2. Coordinates of layer boundaries z_j and coordinates in one repetition period ξ_j.

For real samples several factors (reducing "the density of the nuclear resonant interaction") can decrease the dynamical effects in the reflectivity spectrum, such as the splitting and the broadening of the resonant lines, the relative thickness of the resonant layers in the repetition period, or a dilution of the resonant nuclei density by nonresonant atoms due to intermixing, oxidation, hydrogenation, etc., of the layers. For a given sample, a simple way of decreasing the dynamical interaction (and, hence, simplifying the interpretation of the reflectivity spectra) is a small shift of the angle from the exact Bragg position. However, the reduction of the speed-up and dynamical beat effects in the reflectivity spectra is not the only effect appearing with variation of the angle in vicinity of the Bragg peak. We shall return to this question in Sec. VIII.

III. REFLECTIVITY FROM A PERIODIC STRUCTURE

For a periodic multilayer we can extract the repeated part in Eqs. (11) and (12) by writing

$$z_j = nD + \xi_j \tag{13}$$

where D is the repetition period of the structure and ξ is the z coordinate within each period (Fig. 2). Equation (12) is then expressed as

$$R = \frac{1}{4\sin^2\vartheta}(1+e^{iQD}+e^{2iQD}+e^{3iQD} + \cdots + e^{(N-1)iQD})\sum_{j=1}^{J}(\chi_{j-1}-\chi_j)e^{iQ\xi_{j-1}}, \tag{14}$$

where N is the number of periods in our structure. The sum over j refers to the J boundaries within one period and we can define a structure factor of the "unit cell:"

$$F = \frac{1}{4\sin^2\vartheta}\sum_{j=1}^{J}(\chi_{j-1}-\chi_j)e^{iQ\xi_{j-1}}. \quad (15)$$

The geometrical progression in Eq. (14) is the famous Laue function L_N:

$$L_N = (1 + e^{iQD} + e^{2iQD} + e^{3iQD} + \cdots + e^{(N-1)iQD}) = \frac{1-e^{iNQD}}{1-e^{iQD}} \quad (16)$$

and the reflectivity from the periodic multilayer is expressed as

$$R = L_N(\vartheta, D)F(\vartheta, d_j, \chi_j). \quad (17)$$

Finally we have obtained the following essential features of the simplest kinematical approximation (12) in a periodic structure. The Laue function L_N depends only on the angle ϑ, the repetition period D of the structure, and the number of periods N. At the exact Bragg conditions $QD = n \times 2\pi$, and we have simply $L_N = N$. The variation of this function with the angle is well known. It determines the shape of the Bragg peak. It is essential to notice that the Laue function changes rapidly with small angle variations near the Bragg maximum (ϑ is multiplied by N), while the structure factor varies very slowly. All peculiarities of the spectra, structural information, and in particular their depth selectivity on the scale of one repetition period are contained in the structure factor F [Eq. (15)] [or see further Eq. (21)]. Hence, in this simplest kinematical limit (12) we have almost no variation of the spectrum shape in the vicinity of the Bragg peak but only the usual intensity reduction. However, if the resonant susceptibility is included in the phase factors in Eq. (14), as in Eq. (11), the nuclear resonant interaction will introduce additional effects that will be described later in Sec. VIII.

IV. REFLECIVITY AS A SUM OF WAVES SCATTERED BY SEPARATE SUBLAYERS

Formulas (11), (12), (14), and (15) determine the reflectivity as a sum of waves reflected by the boundaries between two continuous media and each item in the sum depends on both adjacent layers. In the further experimental data analysis we will try to distinguish the properties of the nuclear scattering amplitude with respect to different hyperfine interactions in each sublayer and it is appropriate to rewrite Eq. (15) by introducing the scattering from a set of discrete thin layers. The scattering amplitude r from a single scattering plane can be obtained from Eq. (12) if we put

$$\chi_{j-1} = 0, \quad \chi_{j+1} = 0, \quad \chi_j = \frac{\lambda^2}{\pi}\rho_j f_j, \quad (18)$$

which gives

$$r = \frac{1}{4\sin^2\vartheta}[(\chi_{j-1}-\chi_j) + (\chi_j - \chi_{j+1})e^{iQd_j}] \approx \frac{iQd_j}{4\sin^2\vartheta}\chi_j. \quad (19)$$

Defining the surface density of the scattering centers as $\sigma_j = \lim_{d_j \to 0}(\rho d_j)$ we obtain the well-known expression for the reflection amplitude from a single plane (see, e.g., Refs. 51 and 52)

$$r = i\frac{\lambda}{\sin\vartheta}\sigma f. \quad (20)$$

Because the dominating real part of the atomic scattering amplitude f is negative in the x-ray region this formula implies that the scattered wave lags the incident wave by $\pi/2$. Now the structure factor (15) can be expressed as

$$F = \frac{i\lambda}{\sin\vartheta}\sum_{k=1}^{K}\sigma_k f_k e^{iQ\xi_k}, \quad (21)$$

where k numerates the discrete sublayers in the unit cell. Equation (21) allows us to analyze how separate sublayers contribute to the total reflectivity signal (in the kinematical limit).

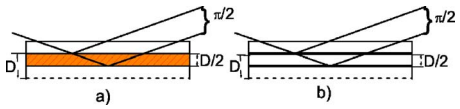

FIG. 3. (Color online) The illustration of the difference of the reflectivity calculated by the formulas (15) and (21). In both cases we add two waves with the same space phase shift $Q\xi = \pi$. But Eq. (15) describes the reflectivity by two boundaries between continuous media (a) and Eq. (21) describes the reflectivity by two thin layers in empty space (b).

At first sight the two expressions (15) and (21) are quite similar. For illustration of their difference let us consider only two terms in each of them with the same phase difference, e.g., $Qd = \pi$. The first formula (15) gives the reflectivity from a layer with susceptibility χ and adds the waves reflected from two boundaries [Fig. 3(a)]

$$F = \frac{1}{4\sin^2\vartheta}[(\chi_1 - \chi_2) + (\chi_2 - \chi_1)e^{i\pi}]$$
$$= \frac{1}{4\sin^2\vartheta}(-\chi + \chi e^{i\pi}) = \frac{-\chi}{2\sin^2\vartheta}. \quad (22)$$

At $Qd = \pi$ we get the maximum reflectivity. The expression (21) adds two waves from two infinitely thin layers in the unit cell [Fig. 3(b)]:

$$F = \frac{i\lambda}{\sin\vartheta}(\sigma_1 f_1 + \sigma_1 f_1 e^{i\pi}) = 0 \quad (23)$$

and at $Qd = \pi$ we get the total suppression of the reflection. In both cases Eqs. (15) and (21) we have two adding waves. But the model and the result is quite different. In order to get the result (22) by formula (21) it is necessary to consider another model, namely, to fill the layer by a continuous set of sublayers:

$$F = \frac{i\lambda}{\sin\vartheta}\sigma^{\mathrm{diff}} f\int_0^d e^{iQ\xi}d\xi = \frac{-\chi}{2\sin^2\vartheta} \quad (24)$$

if we define the differential surface density as $\sigma^{\mathrm{diff}} = \rho$ and put $Qd = \pi$.

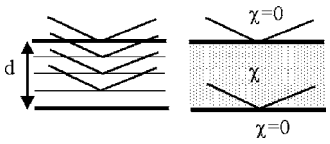

FIG. 4. Reflectivity from discrete (atomic) layers (left side) and reflectivity from continuous thick layer (right side).

Here another question arises: how thin should these sublayers be in order to simulate the continuous layer model, and vice versa, how good an approximation is the continuous medium model in reflectivity theory for discrete atomic (or even more thin nuclear) layers in epitaxially grown films.

Consider the reflection by n equal layers with a total thickness of d (see Fig. 4). In the continuous model [Eq. (15)] the scattering by a layer in vacuum having the susceptibility χ with thickness of d gives

$$F = \frac{-\chi}{4\sin^2\vartheta}(1 - e^{iQd}). \tag{25}$$

Supposing that in reality we have in this layer the set of n discrete (atomic) planes with surface density $\sigma = \rho d/n$ we instead have from Eq. (21)

$$F = \frac{i\lambda}{\sin\vartheta}\sigma f\sum_{k=0}^{n-1} e^{iQkd/n} = \frac{i\lambda}{\sin\vartheta}\sigma f\frac{1 - e^{iQd}}{1 - e^{iQd/n}}$$

$$\approx \frac{-\chi}{4\sin^2\vartheta}(1 - e^{iQd}). \tag{26}$$

The approximation in Eq. (26) is valid if $Qd/n \ll 1$ and $e^{iQd/n} \approx 1 + iQd/n$ which implies that

$$\sin\vartheta \ll \frac{\lambda}{4\pi d/n}. \tag{27}$$

Hence, for angles that are much smaller than the Bragg angle for a given lattice spacing d/n, the continuous approach is appropriate also for electronic and nuclear resonance scattering.

In the qualitative analysis below we shall use mainly the expression (15) for the electronic contribution to the scattering but expression (21) for the nuclear resonant contribution, because it is essential to select different resonant contributions according to their depth position.

V. STUCTURE SENSITIVITY OF THE REFLECTIVITY IN THE SIMPLEST KINEMATICAL APPROXIMATION

Using the kinematical limit formula (21) for the structure factor, neglecting the refraction corrections in the phases of the separate contributions, we can qualitatively analyze the site sensitivity of the Bragg reflectivity and compare the results for the energy and time domains. As illustrations we consider some significant model examples.

The first one shows how the phase shift in the time-spectrum quantum beat oscillations changes with the position of the resonant layer in the repetition period. Consider a simple repetition period where two thin resonant sublayers

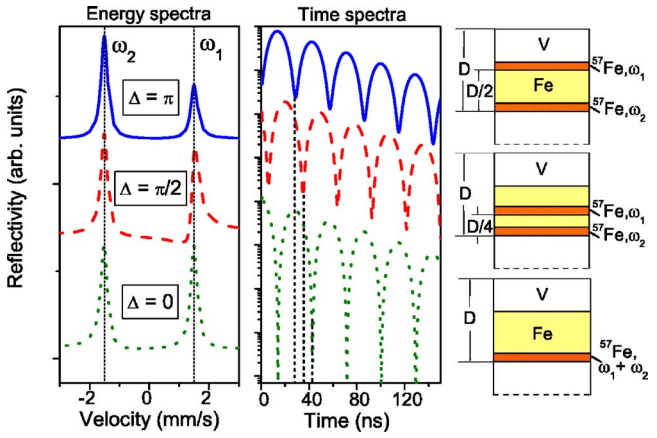

FIG. 5. (Color online) The structure sensitivity of the Bragg reflectivity is illustrated. The relative positions of two ^{57}Fe monolayers in an [Fe/V] structure leads to a change in the ratio of the line intensities in the energy spectra and to a phase shift of the quantum beat oscillations in the time spectra. This phase shift is easily detected in an experiment.

(^{57}Fe) with equal thickness d are placed at the depths ξ_1 and ξ_2. For simplicity we also assume that each resonant layer is characterized by a single resonance frequency (ω_1 and ω_2, respectively). The corresponding structure factor is

$$F(\omega) = F^{\mathrm{el}} - \frac{id}{2\sin\vartheta}\mu^{\mathrm{nuc}}\left(\frac{\Gamma/2\hbar}{\omega - \omega_1 + i\Gamma/2\hbar}e^{iQ\xi_1} + \frac{\Gamma/2\hbar}{\omega - \omega_2 + i\Gamma/2\hbar}e^{iQ\xi_2}\right), \tag{28}$$

where F^{el} is the structure factor for the scattering by the electronic density, including contributions from nonresonant layers and independent of the energy shifts across the resonant spectrum. The time dependence of the structure factor is calculated by applying the Fourier transform

$$F(t) = \frac{1}{2\pi}\int_{-\infty}^{+\infty} F(\omega)e^{-i\omega t}d\omega. \tag{29}$$

The electronic scattering F^{el} now disappears and for each resonant line we obtain a decaying wave with a resonance frequency $\omega_0 = \omega_{1,2}$:

$$\frac{1}{2\pi}\int_{-\infty}^{+\infty}\frac{e^{-i\omega t}}{\omega - \omega_0 + i\Gamma/2\hbar}d\omega = ie^{-i\omega_0 t - \Gamma t/2\hbar}. \tag{30}$$

Omitting some trivial factors we can write the structure factor in the time representation as

$$F(t) \propto e^{-\Gamma t/2\hbar}(e^{iQ_1\xi_1 - i\omega_1 t} + e^{iQ_2\xi_2 - i\omega_2 t}) \tag{31}$$

and the corresponding intensity of the reflected wave as

$$|F(t)|^2 \propto 2e^{-t/\tau_0}[1 + \cos((\xi_1 - \xi_2)Q + (\omega_2 - \omega_1)t)], \tag{32}$$

where $\tau_0 = \hbar/\Gamma$ is the mean lifetime. This result is quite similar to the time spectra of two resonant nuclei in forward scattering[21] but with one very essential difference. In the delayed decay curve (Fig. 5) an additional phase shift $\Delta = (\xi_1 - \xi_2)Q$ of the quantum beat oscillations appears (we

shall call it as a "space phase shift"). Since this phase shift depends on the distance $(\xi_1-\xi_2)$ between the resonant sublayers within a repetition period it grants a possibility for an experimental determination of the depth distribution of the magnetic structure. The spectra shown in Fig. 5 were calculated for a $[\mathrm{Fe}(1.8\ \mathrm{nm})/\mathrm{V}(1.2\ \mathrm{nm})]_{20}$ model structure. The two resonant ^{57}Fe layers with thicknesses $d=0.3$ nm and enrichment $P=0.5$ were placed at different depths ξ in the nonresonant ^{56}Fe layer. Their single resonance energies correspond to (±1.5 mm/s isomer shifts in the Mössbauer spectrum. At the first Bragg peak ($\vartheta_B=14.75$ mrad) the bilayer depth $D=3$ nm corresponds to a 2π phase shift and the phase shift Δ in the time spectra can be calculated in units of 2π as $[(\xi_1-\xi_2)/D]2\pi$. Hence, $Q(\xi_1-\xi_2)=\pi$, $\pi/2$, and 0 for the three cases presented in Fig. 5, respectively, from the top to the bottom. For the computer simulations we actually used the general Parratt formula (1), taking into account the refraction effects as well, but the main features of the spectra can be explained by a qualitative analysis in the simplest kinematical approximation.

It is interesting that in order to explain the variation of the relative intensities of lines in the energy spectra in Fig. 5 we must also take into account the electronic part of the scattering F^{el}. For example, for the case when the two resonant sublayers are separated by $D/2$, the electronic and nuclear resonant scattering are added in antiphase for the $\omega_1=+1.5$ mm/s line ($\mathrm{Re}(\chi_{\mathrm{V}}-\chi_{\mathrm{Fe}})>0$, $F^{\mathrm{nuc}}(\omega=\omega_1)\propto i^2\,\mathrm{Im}[f^{\mathrm{nuc}}(\omega=\omega_1)]<0$), so their interference is destructive. We use Eq. (21) for the description of the contributions from thin sublayers, but Eq. (15) for the electronic contributions from thick layers. The ω_2 line is enhanced by a constructive interference with the electronic scattering because the contribution from the resonant sublayer with $\omega_2=-1.5$ mm/s gets the additional phase shift π and $\mathrm{Re}(\chi_{\mathrm{Fe}}-\chi_{\mathrm{V}})>0$. When the space phase shift for the sublayer with the ω_1 line becomes $\pi/2$ (Fig. 5, middle case), the real part of $f^{\mathrm{nuc}}(\omega=\omega_1)$, having different signs on both sides of the exact resonance, interferes with F^{el} which results in a noticeable asymmetry of the reflectivity at the ω_1 line. Hence, in the simplest kinematical approximation the energy spectra are sensitive to the different positions of the resonant layers relative to the electronic structure while the time spectra depend only on the distance between resonant layers. However, later we will show that if refraction effects are included the information on the position of the resonant layers relative to the electronic structure appears also in the time spectra.

From the previous discussion and Eq. (30) it is evident that two identical resonant sublayers, at a separation $(\xi_1-\xi_2)$ of half a multilayer period, interfere destructively at the first Bragg peak since $Q(\xi_1-\xi_2)=\pi$. In our next model example we use a $[\mathrm{V}(1.5\ \mathrm{nm})/^{57}\mathrm{Fe}(1.5\ \mathrm{nm})]_{20}$ multilayer assuming that a $\frac{1}{4}$ iron layer at both interfaces has a smaller hyperfine field (21 T) than that in the middle part of the ^{57}Fe layer (33 T). For simplicity we also assume that the hyperfine fields are orientated perpendicular to the layers so only two lines (second and fifth) in each sextet are excited by the σ-polarized radiation. We choose the same relative amount of resonant nuclei with each kind of hyperfine field (33 and 21 T). A conventional absorption Mössbauer spectrum then shows two doublets with equal amplitudes of all four lines.

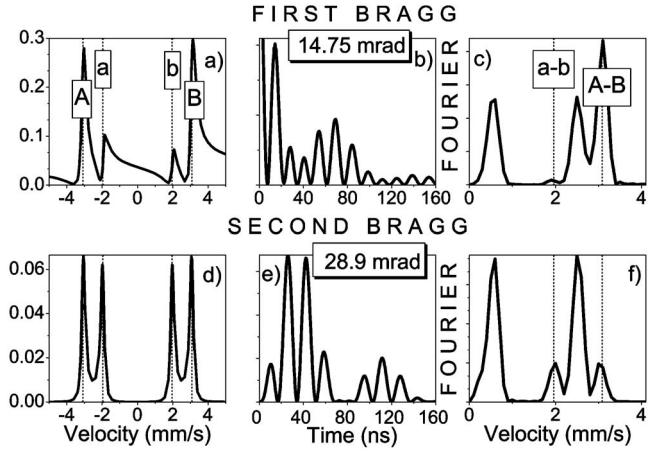

FIG. 6. Energy spectra (a),(d), the corresponding reflectivity time spectra (b),(e) and their Fourier transforms (c),(f) calculated at the first- and second-order Bragg peaks. Details of the structure are explained in the text. The frequency scale of the Fourier transform is rescaled in order to allow a direct comparison with the velocity (energy) scale of the Mössbauer spectrum.

In the energy spectrum of reflectivity at the first-order Bragg peak [see Fig. 6(a)] we observe the substantial suppression of the lines (denoted *a* and *b* in Fig. 6), corresponding to the interface field (21 T), and the disappearing of the beat frequency between those lines $(a-b)$ in the time spectrum. As already mentioned this is due to the destructive interference of the two interface contributions with a phase difference of $\Delta=Q(\xi_1-\xi_2)\approx\pi$. At the second-order Bragg peak this phase difference is instead 2π and all lines in the energy spectrum are present with comparable intensities. However, both time spectra of reflectivity, and in particular at the second-order Bragg peak, are dominated by the beating between the two hyperfine fields: interference of the lines *A*-*b* and *B*-*a* gives the maximum at 2.5 mm/s in the half-frequency-scaled Fourier transforms of the time spectra in Fig. 6. This also illustrates how much more complicated the interpretation of the time spectrum may be compared to the energy spectrum.

The analysis of the frequency contributions in the time spectrum is not as straightforward as for the different lines in the energy spectrum. Here and later on we have used the Fourier transform of the reflectivity time spectra in order to identify the different beat frequencies. We calculate the Fourier transform using a Kaiser-Bessel window function

$$W(n)=I_0[\beta\sqrt{1-(n/N)^2}]/I_0(\beta) \tag{33}$$

based on modified Bessel functions of the first kind (β is a shape parameter). A previous normalization of the time curve to a fitted decay factor often gives a better resolution of the beat frequencies, in particular in the low-frequency range, but on the other hand prevents comparisons of intensities between different time spectra.

In our first model example (Fig. 5) we used two singlet resonant lines to illustrate how the scattering phase difference, caused by the different positions of resonant sublayers

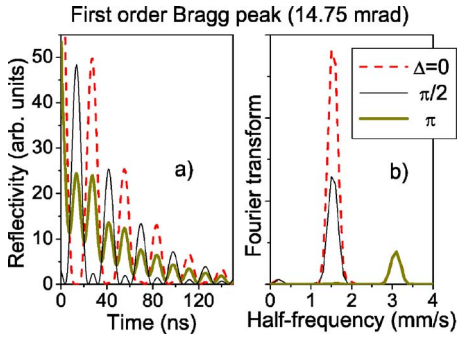

FIG. 7. (Color online) Time spectra of reflectivity (a) and their Fourier transforms (b) for three different relative positions of two thin resonant ^{57}Fe layers, having $\mathbf{B}_{\mathrm{hf}}$=33 and 0 T, respectively, in a $[\mathrm{V/Fe}]_n$ superstructure. The layers are placed at 0, 1/4, and 1/2 the distance of the repetition period corresponding to a space phase difference of the reflectivity amplitudes $\Delta=0$ (solid lines), $\pi/2$ (dashed lines), and π (dotted lines). The Fourier transforms are normalized to the peak at 3 mm/s, which corresponds to interference of the second and fifth lines in the 33 T spectrum. The 1.5 mm/s peak corresponds to the interference of these second and fifth lines with the singlet line. The frequency scale of the Fourier transform is rescaled in order to allow a direct comparison with the velocity (energy) scale of the Mössbauer spectrum.

in the repetition layer, directly appears in the reflectivity energy and time spectrum. As more Mössbauer lines are present these space phase shifts will enhance or suppress various cross-interference beats. In the next example we replace one of the singlets by a doublet from a 33 T hyperfine field again oriented perpendicular to the layer surface for simplicity (only Mössbauer lines 2 and 5 are excited by linearly polarized synchrotron radiation). The time-dependent structure factor then contains three waves with amplitude A_B (frequencies ω_1 and ω_2) and A_0 (frequency ω_0), respectively,

$$F(t) \propto e^{-\Gamma/2\hbar}[A_B(e^{-i\omega_1 t}+e^{-i\omega_2 t})e^{iQ\xi_1}+A_0 e^{-i\omega_0 t+iQ\xi_2}]. \tag{34}$$

In the time spectra two frequencies are present. In addition to the beat frequency $(\omega_1-\omega_2)$ corresponding to the energy difference between two lines in the 33 T split spectrum [the 3 mm/s line in Fig. 7(b)], the interference between these transitions and the singlet resonance gives a beat with half the frequency $[(\omega_1+\omega_2)/2=\omega_0$ for no isomer shifts]:

$$|F(t)|^2 \propto e^{-t/\tau_0}\left(A_0{}^2+2A_B^2[1+\cos(\omega_1-\omega_2)t]\right.$$
$$\left.+4A_0A_B\cos\frac{(\omega_1-\omega_2)t}{2}\cos\Delta\right) \tag{34'}$$

where $\Delta=(\xi_1-\xi_2)Q$ is again the space phase shift between the two reflection amplitudes from the resonant layers in the unit cell. The existence and the phase of these half-frequency beats is determined by $\cos\Delta$. Cross-interference beats (at $\sim$1.5 mm/s in the half-frequency scale of the Fourier transform) can appear, disappear, or change sign depending on the relative space position of the resonant sublayers (Fig. 7).

It is easily understood that in general the beat frequencies corresponding to each kind of hyperfine splitting do not depend on the space phase shifts, so they do not change the phase of the oscillations at any angle. They can only be enhanced or suppressed due to the space distribution of the relevant nuclei. The beat frequencies corresponding to the interference between resonant lines of different hyperfine splitting (cross-interference terms) always have a space phase shift of the quantum beats $\Delta_{ij}=(\xi_i-\xi_j)Q$. In principle, space phase differences can be deduced from just one reflectivity time spectrum, provided the frequency components are resolved. However, cancellation of certain fractions may occur (if the phase difference happens to be close to π). Reflectivity time spectra measured at different angles should provide more reliable information (unless the hyperfine fields are distributed homogeneously in the multilayer—which in reality is not probable). The reflectivity time spectra at the critical angle and at the Bragg peaks of different orders reveal drastic differences just because $\Delta_{ij}=\Delta_{ij}(Q)$.

Notice that contrary to the reflectivity time spectrum, the reflectivity energy spectra are not influenced by these cross-interference terms if resonance lines are well separated. The lines are distorted only by the interference with the electronic scattering while in the time representation the electronic scattering does not appear (in the simplest kinematical approximation). That is the essential difference of the two representations.

VI. EXPERIMENTAL APPLICATIONS: RESULTS IN THE SIMPLEST KINEMATICAL APPROXIMATION

The selectivity of the different spectrum contributions with respect to the position of the corresponding scatterers in the repetition period of a multilayer is the particular property of Bragg reflectivity spectra that can be effectively used for a depth structure analysis. An excellent example of such investigations was presented in Ref. 39 where the depth profiles of the magnetic moments of Ce and La across the repetition period were determined by the analysis of the x-ray resonant spectra of the Bragg reflectivity near $L_{2,3}$ edges at nine orders of reflection from periodic Ce/Fe and La/Fe multilayers, respectively.

MgO(001)/[^{57}Fe(6 ML)/Co(3 ML)]$_{35}$/V(10 ML), where ML indicates a monolayer, denoted $[\mathrm{Fe_6Co_3}]_{35}$, was studied by conversion electron Mössbauer spectroscopy and by the time spectra of nuclear resonance scattering in grazing-incidence reflection geometry.[53] The SR measurements were performed at the Nuclear Resonance Beamline of the European Synchrotron Radiation Facility (ESRF). The experimental station is described, e.g., in Ref. 20. CEMS data could be fitted with two hyperfine fields 36.4 and 33.8 T. The low-field value is close to the field in α-iron and it is tempting to assign this field to the monolayers in the center of the Fe layers. However, the fraction (9%) corresponds to only half a monolayer, indicating an interface site. This is also what the SR reflectivity time spectra unambiguously show (see Fig. 8). A beat frequency corresponding to 33.8 T is clearly too small to fit the data. While CEMS probes all ^{57}Fe sites in the sample, nuclear resonance reflectivity at the

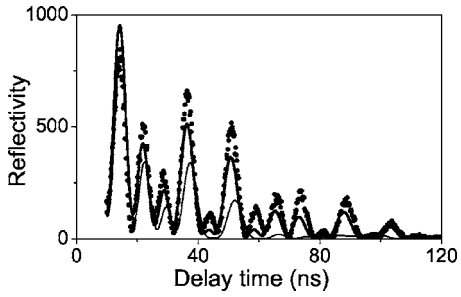

FIG. 8. $[Fe_6Co_3]_{35}$ time spectrum measured at the first-order Bragg peak. The thick full line is calculated with the CEMS parameters and with the low field (33.8 T) in the Co/Fe and Fe/Co interfaces. For the thin line the low field is instead in the center of the Fe layers. The fields are oriented in the layer, along the ⟨110⟩ direction being perpendicular to the beam ($\|e^{\sigma}$).

first-order Bragg angle emphasizes the contribution from the center of the Fe layers, as was shown in the previous section.

Nuclear resonant reflectivity time spectra in the first- and second-order Bragg peaks were measured for the sample MgO(001)/V(5 ML)/$[^{57}$Fe(7 ML)/V(5 ML)$]_{20}$/V(5 ML), denoted $[Fe_7V_5]_{20}$. Measurements were performed in remanence with the sample magnetized along the beam propagation. The experiment was performed at 10 K, and CEMS data for this temperature were not available.

A simultaneous fit of the two Bragg-angle time spectra (Fig. 9) gives us the depth distribution of the hyperfine fields within the repetition of the superstructure, using a model (Fig. 10) with one average field attributed to each ^{57}Fe atomic sublayer.[54] Calculations were performed on the basis of the full theory.[15,35,36,46,47] The result demonstrates a depth selectivity up to one monolayer of the nuclear resonant spectroscopy at Bragg maxima.

Similar investigations but just with one Bragg maximum were done also for other ^{57}Fe/V multilayers.[55] The reflectivity for these systems is relatively high, so some dynamical features (or at least the refraction and absorption corrections) are essential. In particular, they lead to a variation of the spectrum shape in the vicinity of the exact Bragg angle which was used to derive the additional structure information. These results are presented in Sec. XI after a discussion of the refraction and absorption corrections.

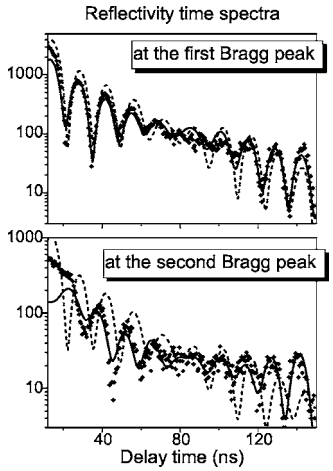

FIG. 9. Time spectra of reflectivity measured for a $[Fe_7V_5]_{20}$ sample at the first- and second-order Bragg peaks; symbols represent the experimental data, solid lines are the fit result giving the model of the hyperfine field depth distribution presented in Fig. 10, and dashed lines are the calculated spectra assuming the same hyperfine fields homogeneously distributed in the whole ^{57}Fe layer. We see that this last model is unacceptable.

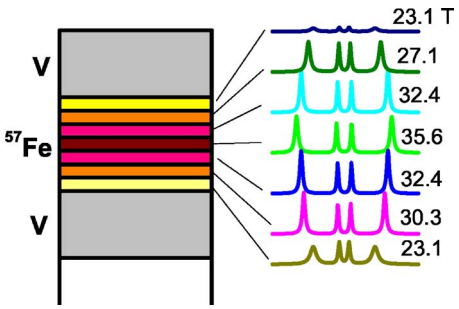

FIG. 10. (Color online) Mössbauer subspectra of the different sublayers in a repetition period of the $[^{57}Fe_7V_5]_{20}$ superstructure, obtained by the fit of the two Bragg reflectivity time spectra presented in Fig. 9.

VII. RESONANT REFRACTION AND ABSORPTION CORRECTIONS

Up to now we have only considered the effects in the simplest kinematical approximation, which can be described by a simple interference of waves reflected by sublayers in one repetition period, that is, by the structure amplitude. The refraction and absorption described by the exponent of Eq. (11) belong to the next order of corrections, but they can lead to noticeable effects in some cases. In the next example we tune the interference conditions in such a way that small refraction corrections will be clearly seen. The model is similar to that of the previous examples (Figs. 5–7 but now with three equidistant thin resonant layers in the repetition period at ξ_1, ξ_2, ξ_3 ($\xi_1 - \xi_2 = \xi_2 - \xi_3$). Layers 1 and 3 are characterized by the doublet (ω_1, ω_2) and layer 2 by the single resonance frequency ω_0, with ω_0 in the middle between ω_1 and ω_2 ($\omega_1 - \omega_0 = \omega_0 - \omega_2$). Omitting the decay factor $e^{-t/2\tau_0}$ we obtain

$$F(t) \propto (e^{-i\omega_1 t} + e^{-i\omega_2 t})(e^{iQ\xi_1} + e^{iQ\xi_3}) + Ae^{-i\omega_0 t + iQ\xi_2}, \quad (35)$$

where A is the relative amplitude of the singlet resonance contribution. The corresponding intensity is given by

$$|F(t)|^2 \propto |A|^2 + 4[1 + \cos(\omega_1 t - \omega_2 t)][1 + \cos(\xi_1 Q - \xi_3 Q)] + 8A \cos\frac{\omega_1 t - \omega_2 t}{2} \cos\frac{\xi_1 Q - \xi_3 Q}{2}. \quad (35')$$

The second term in Eq. (35′) corresponds to the beat frequency $(\omega_1 - \omega_2)$ between the doublet lines and the third term, with half frequency $(\omega_1 - \omega_2)/2$, is the interference term between the singlet line and the doublet lines.

At the exact first-order Bragg angle $Q(\xi_1 - \xi_3) = \pi$ and all quantum beats are suppressed. Only an exponential decay is characterizing the time dependence. This delicate phase equi-

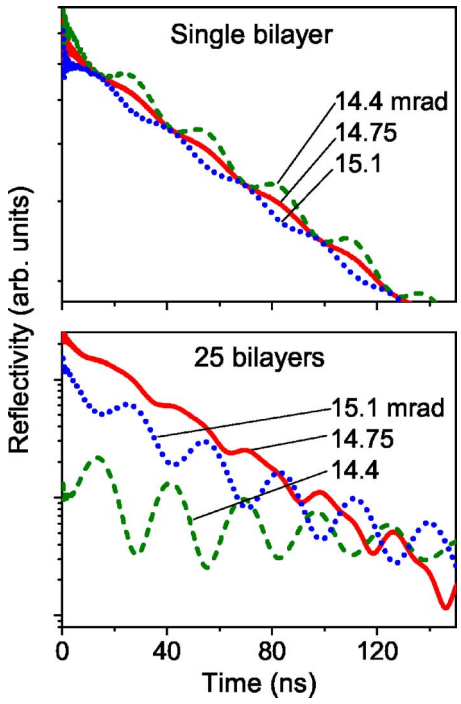

FIG. 11. (Color online) The change of the reflectivity time spectrum with a slight variation of the angle in vicinity of the Bragg peak (ϑ_B=14.75 mrad) calculated for the model described in the text with the superstructure consisting of a single and 25 repetition periods, respectively.

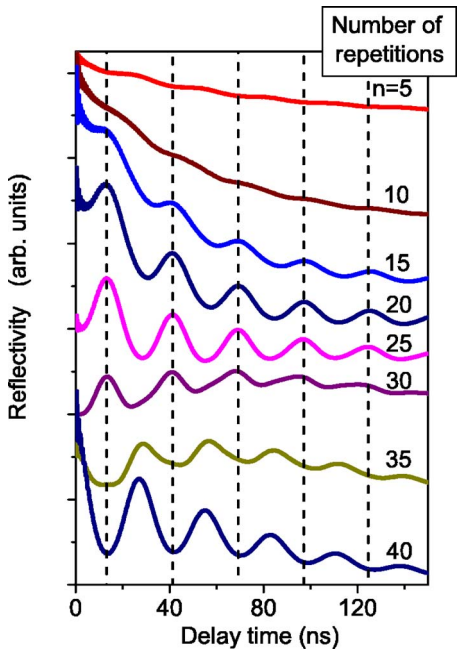

FIG. 12. (Color online) The calculated time spectra of reflectivity at 14.4 mrad for the same model as in Fig. 11, but for a different number of repetitions in the structure. The curves are shifted relative to each other for clearity. The vertical dotted lines are plotted through the maxima of the curve for 25 repetitions in order to follow the oscillation phase reversal.

librium can be destroyed by any imperfection. A small shift of the incident angle off the Bragg peak corresponds to a change in the phase factor $Q(\xi_1-\xi_3)=\pi+\delta$ and the cross-interference term ($\propto\delta$) will dominate compared with the doublet interference beat term ($\propto\delta^2$). We see that these half-frequency beats change the phase by π as the angle is moved through the Bragg angle. This qualitatively explains the calculated time spectra in Fig. 11 where an almost pure single-frequency pattern is seen with opposite phase of oscillations at both sides of the exact Bragg angle. The model used for the calculations is the superstructure $[^{57}\mathrm{Fe}(0.3\ \mathrm{nm})/^{56}\mathrm{Fe}(0.45\ \mathrm{nm})/^{57}\mathrm{Fe}(0.3\ \mathrm{nm})/^{56}\mathrm{Fe}(0.45\ \mathrm{nm})/^{57}\mathrm{Fe}(0.3\ \mathrm{nm})/\mathrm{V}(1.2\ \mathrm{nm})]_n/\mathrm{MgO}$. The density of the resonant ^{57}Fe nuclei in the sublayers 1 and 3, having doublet resonance spectra, was taken three times smaller than that in the sublayer 2 (the single-line resonance layer) in order to enhance the oscillations in the time spectrum. Notice that at the exact Bragg angle the frequency beats are not completely suppressed because in the calculations we take into account the refraction effect, which means that the relative phases of the scattered waves in Eq. (25) are frequency dependent and it is not possible to obtain the exact phase differences π or $\pi/2$ for all frequencies at any angle.

The result of calculations for the structure amplitude (35) directly corresponds to the reflectivity by a single repetition period, as presented in the upper part of Fig. 11. Considering the Laue factor (17) we expect that the variations of the spectra with the angle variation in the vicinity of the Bragg peak will be more pronounced for a larger number of repetitions. Indeed, we see that for 25 repetitions this really takes place (Fig. 11, bottom part), but surprisingly we observe a change of the oscillation phase, compared with single bilayer. Figure 12 shows the reflectivity time spectra calculated for the same model at one and the same angle, off the Bragg peak, but with increasing number of repetitions in the superstructure, and we see that the oscillation phase changes several times. That means that the Laue function in Eq. (17) is not just magnifying the Bragg reflection with the number of repetitions but also changes the spectrum of reflectivity.

Consequently, the expression (16) for the Laue function, which is independent of the resonant factors, should be generalized according to Eq. (11) in order to take into account the resonant refraction and absorption corrections, and we call this approximation the general kinematical approximation. We shall now investigate this approximation more carefully.

VIII. THE LAUE FUNCTION INFLUENCE ON THE ENERGY AND TIME SPECTRA

The separation (17) of the reflectivity amplitude into the structure factor and Laue factor for periodic multilayers is also possible in the general kinematical case when refraction and absorption cannot be neglected in the phase factors. The Laue function then takes the form

$$L_N(\vartheta,D,d_j,\chi_j,\omega)=\frac{1-\exp iN\left(QD+\frac{\kappa}{\sin\vartheta}\sum_{k=1}^{K}\chi_k(\omega)d_k\right)}{1-\exp i\left(QD+\frac{\kappa}{\sin\vartheta}\sum_{k=1}^{K}\chi_k(\omega)d_k\right)}, \tag{36}$$

where K is the total number of the sublayers in one repetition period. The structure factor in the same approximation should be taken as

$$F(\vartheta,d_j,\chi_j,\omega)=\frac{i\lambda}{\sin\vartheta}\sum_{j=1}^{K}\rho_j f_j \exp i\left(Q\xi_{j-1}+\frac{\kappa}{\sin\vartheta}\sum_{k=1}^{j-1}\chi_k(\omega)d_k\right), \tag{37}$$

where $j-1$ is the number of sublayers before the reflecting sublayer j in one repetition period. However, the refraction and reflection corrections in Eq. (37) are not enhanced by the number of the repetition periods N [as in Eq. (36)], so they can be neglected in most cases. The change of the time spectrum in Figs. 11 and 12 for different numbers of the repetition period, determined by the refraction corrections in Eq. (37), is a quite special case.

The most essential consequences for the resonant scattering arise from the energy dependence of the Laue function. In the general kinematical approximation with a separation of the structure factor into a nonresonant F^{el} part describing the scattering by the electrons and a nuclear part F^{nuc} we have the general expression for the reflectivity

$$R(\omega)=F^{\mathrm{el}}L_N(\omega)+F^{\mathrm{nuc}}(\omega)L_N(\omega), \tag{38}$$

or in the time representation

$$R(t)=F^{\mathrm{el}}L_N(t)+R^{\mathrm{nuc}}(t), \tag{39}$$

where

$$R^{\mathrm{nuc}}(t)=\int_0^{\infty}F^{\mathrm{nuc}}(t')L_N(t-t')dt', \tag{40}$$

and the Fourier transform of the Laue function is

$$L_N(t)=\frac{1}{2\pi}\int_{-\infty}^{+\infty}L_N(\omega)e^{-i\omega t}d\omega. \tag{41}$$

Let us first analyze the results in the energy representation. Remember that the Laue function changes quickly with a small angle variation in the vicinity of the Bragg peak. So the nuclear resonant reflectivity spectra (38) will distinctively change shape while the angle is shifted across the Bragg maximum. For one resonant line it was shown in Ref. 19.

The structure factor (37), Laue function (36), and total reflectivity curve (17) are compared in Fig. 13 for our first model example used for Fig. 5 with two sublayers with singlet resonant lines ω_1 and ω_2 in each one. There is no visible change of the structure factor with a small variation of the angle, but we see that the Laue function changes drastically. A significant distortion of the reflectivity line shapes, different for different angular shifts in the vicinity of the Bragg peak, is caused by the Laue function. We obtain a line broadening, even a splitting, and a substantial asymmetry of the lines. The effects are quite similar to those observed for thick resonant absorbers, but here the thickness effect is associated with the angle variation through the Laue function. The exponential factor in Eq. (36),

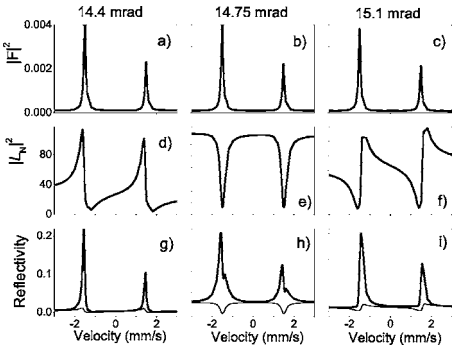

FIG. 13. Energy dependencies of the modulus squared of the structure factor (a),(b),(c), the Laue function (d),(e),(f), and their product (g),(h),(i) giving the reflectivity energy spectrum calculated at three angles in the vicinity of the Bragg maximum. Calculations were done for the same model as used for Fig. 5 but the number of repetitions was taken to be 30. Thin lines in (g),(h),(i) are the electronic contribution to the reflectivity, proportional to the Laue function.

$$\exp\left[iN\left(QD+\frac{\kappa}{\sin\vartheta}\sum_{k=1}^{K}\chi_k(\omega)d_k\right)\right]$$

describes actually the total change of the amplitude and phase of the incident wave during double transmission through the whole multilayer at the glancing angle ϑ.

Such a dispersive resonant absorption is not the only effect caused by the energy dependence of the Laue function. An additional circumstance should be taken into account. This very essential property is that the electronic contribution F^{el} now becomes energy dependent after multiplication by the Laue function (36) and leads to a distortion of the nuclear resonant reflectivity spectra. For each reflectivity spectrum in Fig. 13 the energy-dependent "background line" is also shown, which actually is the electronic scattering contribution, repeating the shape of the Laue function. The effect is quite similar to the distortion of the resonant secondary radiation yield by the nonresonant secondary radiation investigated in Refs. 34–36 and 41 at the total reflection conditions.

In the time representation this electronic contribution not only reveals itself as a prompt electronic response but also in the decay. This additional distributed source of coherent (electronic) scattering having definite resonant frequencies determined by the Laue factor $L_N(t)$ (41), Eq. (36) will interfere with the nuclear resonant scattering and create additional quantum beat oscillations. Hence, the influence of the Laue function on the reflectivity curve in the time representation is considerably more intricate.

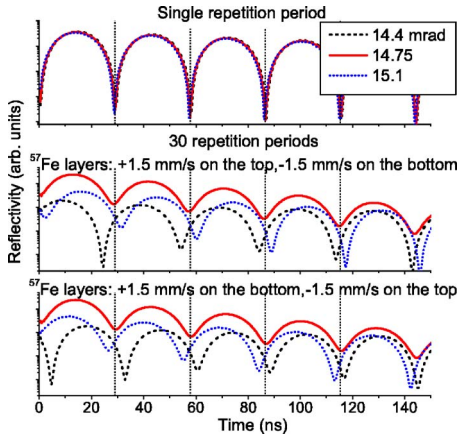

FIG. 14. (Color online) Time spectra of reflectivity calculated for the same model as in Fig. 5 with $\Delta=\pi$ and for a single repetition period (top graph) and 30 repetition periods (below). Three angles at the Bragg maximum are considered. No oscillation phase shift appears for one repetition period but for 30 repetition period it depends on the sequence of the electronic susceptibilities in the multilayer.

The calculated time spectra in Fig. 14 show that for relatively large number of repetitions a significant phase shift of the quantum beat oscillations appears with different signs on either sides of the exact Bragg angle. The origin must be found in the Laue function. A remarkable observation is that if we in the calculations reset the electronic susceptibility in all layers to zero, the phase shift of the quantum beat oscillations disappears. Hence, this phase shift is predominantly caused by the influence of the electronic scattering and in particular by the interference of the electronic (modified by the Laue function) and nuclear resonant reflectivity. This conclusion is supported by the result shown in Fig. 14, namely, we see that the phase shift of the oscillations also depends on the positions of the resonant sublayers *relative to the electronic structure*. So in the general kinematical approximation the electronic scattering participates in the reflectivity time spectra as well as in the energy spectra (contrary to the simplest kinematical approximation) and it suggests an additional structure sensitivity introduced by the Laue function.

This additional time dependent electronic scattering is the reason for the reversal of the phases of the quantum beat oscillations in Fig. 12. The dominating frequency there is $(\omega_1-\omega_2)/2$, which is the result of the interference of the ω_0 component with the ω_1 and ω_2 components being almost completely suppressed in the structure factor. But the frequency components ω_1 and ω_2 become more and more enhanced with increasing number of repetitions N—through the Laue function, multiplying the electronic scattering amplitude in particular—and now they can interfere with the ω_0 component. These electronic ω_1 and ω_2 resonant scattering amplitudes can change phase for different N as shown in Fig. 15, whereas the change in the nuclear resonant scattering amplitude is negligible. That explains the results shown in Fig. 12.

In the energy representation the reflectivity line shape is described by a simple product of the structure factor and the

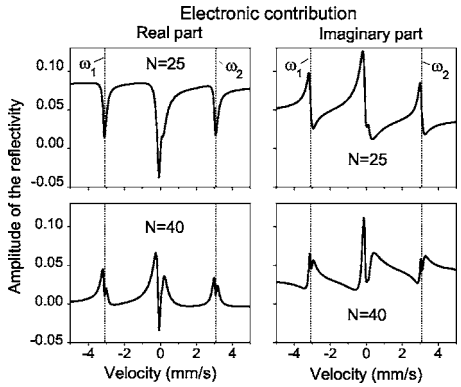

FIG. 15. The energy dependence of the real and imaginary parts of the electronic reflectivity amplitude, calculated for the same model as in Fig. 12 and at an angle of 14.4 mrad. The electronic amplitude changes sign (or phase by π) at resonant energies at ω_1 and ω_2 when the number of periods increases from 25 to 40. This explains the reversal of the oscillation phase observed in Fig. 12.

Laue function [see Eq. (38)] which can readily be studied separately. In the time representation the reflectivity is described as a convolution of the Fourier transforms of the nuclear structure factor and the Laue function (40). In such an integral form it is difficult to analyze the results on a qualitative level. Some more understanding can be achieved if we instead consider the differential contributions to the reflectivity signal from selected sublayers.

IX. THE INFLUENCE OF STANDING WAVES ON THE REFLECTIVITY

The Laue function describes how the number of repetitions in a multilayer influences the reflectivity and we find that in the general kinematic approximation the spectrum shape of the total reflectivity is not simply a multiplicative factor times the shape for a single repetition period. Hence, the contribution to the reflectivity from each individual sublayer in a periodic multilayer depends somehow from the other layers. The multilayer creates a collective excitation state which influences the reflectivity from each single layer. The Laue function describes only the total effect of all layer contributions, which of course is what the measurements give, but from a fundamental point of view it is also interesting to know how the reflectivity changes when we put a particular single layer into the multilayer structure.

Consider first the simple example with a thin resonant layer on the top of some multilayer structure, here called the "substrate" (not to be confused with the substrate on which a multilayer is grown). Without the resonant layer, the reflected wave at a distance H from the surface of the reference substrate, normalized to the incident wave at the same position H, is

$$R = R^{\text{substr}} e^{iQH}, \tag{42}$$

where R^{substr} is the reflectivity on the top of the substrate. When we add a thin resonant layer with susceptibility χ and thickness d at the distance H from the surface, the total reflectivity within the general kinematical approximation [compare with Eqs. (11) and (37)] becomes

$$R^{\mathrm{tot}} = Re^{i(2\pi\chi/\lambda \sin \vartheta)d} + r, \tag{43}$$

where we take into account the refraction corrections for the incident and reflected waves twice crossing the added layer. The reflectivity from this thin layer is [see Eq. (20)]

$$r = i\frac{\pi\chi}{\lambda \sin \vartheta}d. \tag{44}$$

Assuming the thickness d is small, a first-order expansion of the exponential factor in Eq. (43) gives the following simple expression for the contribution to the total reflectivity caused by the additional layer:

$$R^{r} = R^{\mathrm{tot}} - R = r(1 + 2R^{\mathrm{substr}}e^{iQH}). \tag{45}$$

At the exact Bragg angle for the periodic multilayer the phase of e^{iQH} in Eq. (45) passes a full period when H changes in one repetition period. So depending on the position z the contribution from a thin sublayer to the total reflectivity may be enhanced or suppressed by a factor of $1 \pm 2|R|$, respectively. Notice that this factor cannot be negative, since $R \ll 1$ in the kinematical approximation.

Equation (45) is in direct analogy to the x-ray standing-wave method,[56,57] where the intensity of the secondary (e.g., fluorescent or photoelectron yield) radiation depends on the position of the emitting atoms relative to the nodes or antinodes of the standing waves, created by the coherent superposition of the incident and reflected waves. A remarkable difference is that the amplitude of the secondary radiation is proportional to $(1+R)$, whereas we here obtain $(1+2R)$.

The origin and interpretation of this difference become clear when the consideration is performed exactly—in the dynamical approximation on the basis of Eq. (1).[25] For calculations of the reflectivity from a thin layer by Eq. (1) we assume that the phase shift $2i\varphi$ due to the thin layer, placed at the distance H from the substrate surface, is small. Neglecting $(2i\varphi)^2$ term we obtain

$$R^{\mathrm{tot}} = \frac{r_{01} + \tilde{R}}{1 + r_{01}\tilde{R}} + \frac{\tilde{R}(1 - r_{01}^2)}{(1 + r_{01}\tilde{R})^2}2i\varphi \tag{46}$$

and

$$\tilde{R} = \frac{r_{10} + R}{1 + r_{10}R}, \tag{47}$$

where r_{01} and r_{10} are the Fresnel reflectivity amplitudes from both sides of the tested layer and R is determined by Eq. (42). Finally we obtain

$$R^{\mathrm{tot}} = R^{\mathrm{substr}}e^{iQ(H+d)} + r(1 + R^{\mathrm{substr}}e^{iQH})^2, \tag{48}$$

where r again is determined by Eq. (44).

So in the exact calculations the contribution to the total reflectivity, caused by the additional layer, is proportional to $(1+R)^2$, but not to $(1+R)$ as occurs for secondary radiation. The kinematical approach (45) obtained above was valid because when R is small, $(1+R)^2 \approx 1+2R$. This result explains the essential difference between the secondary radiation yield and reflectivity from some sublayer. The reflectivity amplitude r in the presence of the other reflecting layers is modulated by the "squared standing wave" $(1+R)^2$ because the standing-wave structure of the radiation field reveals itself for the incident (absorption process) as well as for the reflected wave (emission process). The scattered secondary radiation is not coherent with the incident wave, so we should not take into account the standing-wave structure for the scattered wave.

It is possible to investigate the general case when a thin sublayer with reflectivity r is placed inside a multilayer at a depth z. The previous derivations will be valid for that part of the multilayer which is below the considered sublayer:

$$R^{r}(z) = rT(z)T'(z)[1 + R^{\mathrm{below}}(z)]^2, \tag{49}$$

where $T(z)$ and $T'(z)$ describe the transformation of the wave on the way from the surface to the z position and back. R^{below} is the reflectivity amplitude at the same depth z from all layers below the considered one. In the kinematical approximation we obviously obtain [compare with Eq. (37)]

$$T(z)T'(z) = \exp\left(iQz + \frac{2\pi}{\lambda \sin \vartheta}\sum_{m=1}^{j-1}\chi_m d_m\right), \tag{50}$$

where we take into account the refraction and absorption corrections for the direct and reflected waves and the sum over m is performed for all sublayers in the upper part of multilayer. Direct calculations in the dynamical approximation (1) give the following expression for $T(z)T'(z)$:

$$T(z)T'(z) = e^{2i(\varphi_1+\varphi_2+\cdots+\varphi_{j-1})}\frac{(1 - r_1^2)(1 - r_2^2)\cdots(1 - r_{j-1}^2)}{(1 + r_1R_2e^{2i\varphi_1})^2(1 + r_2R_3e^{2i\varphi_2})^2\cdots(1 + r_{j-1}R_je^{2i\varphi_{j-1}})^2} \tag{51}$$

if the investigated thin layer is at the jth boundary. This expression gives the magnitude of the standing-wave amplitude at depth z and together with Eq. (49) determines the possibility to have much more essential enhancement of the response from a thin investigated layer r if it is placed inside the waveguide layer. Such an enhancement was experimentally attained in Ref. 6. Note that the waveguide enhancement of the field amplitude in, e.g., the $(j-1)$ layer is achieved when

$$1 + r_{j-1}R_je^{2i\varphi_{j-1}} \approx 0. \tag{52}$$

The analysis of such a situation shall be given elsewhere.

Notice that the expression for $T(z)$ is straightforwardly obtained on the basis of Eq. (1):

$$T(z) = e^{i(\varphi_1+\varphi_2+\cdots+\varphi_{j-1})}\frac{(1+r_1)(1+r_2)\cdots(1+r_{j-1})}{(1+r_1R_2e^{2i\varphi_1})(1+r_2R_3e^{2i\varphi_2})\cdots(1+r_{j-1}R_je^{2i\varphi_{j-1}})}. \quad (53)$$

In addition the expression (51) presented here allows us to get an exact expression for $T'(z)$ which is actually the "function of escape" of outgoing radiation penetrating through the top part of a multilayer. In particular, we have from Eqs. (51) and (53)

$$T'(z) = T(z)\frac{\eta_j}{\eta_0}, \quad (54)$$

where η_j is determined by Eq. (2). For derivation of Eq. (54) we take into account that

$$1 - r_i^2 = (1-r_i)(1+r_i) = t_i t_i', \quad t_i = \frac{2\eta_{i-1}}{\eta_{i-1}+\eta_i}, \quad t_i' = \frac{2\eta_i}{\eta_{i-1}+\eta_i},$$

where t_i, t_i' are the Fresnel transmission coefficients through the boundary between the $(i-1)$ and i layers.

The obtained general expression (49) shows that in the kinematical (50) as well as in the dynamical (51) approximation, the dependence $R^r(z)$ on ω (and thus its participation in the delayed signal) can appear in different ways: (i) from the tested layer reflectivity $r=r(\omega)$, but also from the surrounding multilayer if it contains resonant sublayers through (ii) $R^{\text{below}}=R^{\text{below}}(\omega)$ or (iii) $\chi_i=\chi_i(\omega)$ in the top part of the multilayer. In particular the electronic scattering from a nonresonant sublayer r acquires a resonant dependence on being placed inside a resonant multilayer. In the previous section we showed the same with the Laue function.

The standing-wave concept is rather fruitful because it predicts the angular variations of the response from an investigated layer. The position D of antinodes of the standing wave above the reflecting mirror is determined by

$$\arg[R^{\text{below}}(\vartheta)] + \frac{4\pi D}{\lambda}\sin\vartheta = 2\pi n \quad (55)$$

so it is substantially shifted with an angle variation near the Bragg angle and the contribution to the reflectivity from a definite layer will have a maximum at the angle at which the antinodes of the standing wave coincide with the layer position H.

The situation when the multilayer itself is nonresonant but the investigated sublayer is a resonant one, $r=r(\omega)$, is the simplest to analyze. In this case the angular dependence of the delayed nuclear resonant reflectivity is determined from the depth position and thickness of the investigated resonant layer according to the variations of the standing-wave amplitude at the position of the resonant sublayer. For the total external reflection region the angular dependencies were calculated for different depth position of the resonant sublayer in Refs. 58–60. In particular, the electronic standing wave $|(1+R)^2|^2$ explains the existence and the height of the maximum in the angular dependence of the time-integrated delayed resonant reflectivity near the critical angle ("interference peak"), observed in Refs. 22 and 23.

For the periodic multlayer the regular standing-wave structure has the same period as the multilayer itself (at the first-order Bragg peak) which makes it possible to detect the position of the tested sublayer on the scale of one repetition period. As the angle changes in the vicinity of the Bragg peak, the antinodes of the standing wave are shifted across one repetition period and enhance the contribution to the reflectivity from definite layer positions. In such a way "a scan" across the bilayer depth is performed by the angle variation.

A very illustrative example of the standing-wave influence on the nuclear reflectivity was obtained for a $Si/[Mo/Si]_{45}/^{57}Fe/Nb(70\text{ nm})$ sample.[61] The Bragg reflectivity from the nonresonant periodic multilayer "substrate" $[Mo/Si]^*45$ was very strong, being a good generator of a standing wave with the period of the structure ~5.83 nm. The nuclear resonant scattering arose only from one thin ^{57}Fe layer.

The intersection of the antinode of the standing wave with the resonant layer took place at a glancing angle slightly smaller than the exact Bragg angle. That explains the obtained shift and shape of the integral delayed nuclear reflectivity peak. The comparative fit of the prompt and delayed reflectivity curves allowed us to determine the exact position z and thickness d of the ^{57}Fe layer (Fig. 16).

Such a shift of the delayed reflectivity Bragg peak relative prompt peak was noticed in Refs. 62–64 [look below in Fig. 25(a)] but for the resonant multilayer used in that work the interpretation was not so clear as here.

X. RESONANT STANDING WAVES

The most specific case is the resonant periodic multilayer. The concept of standing waves should be reconsidered in this

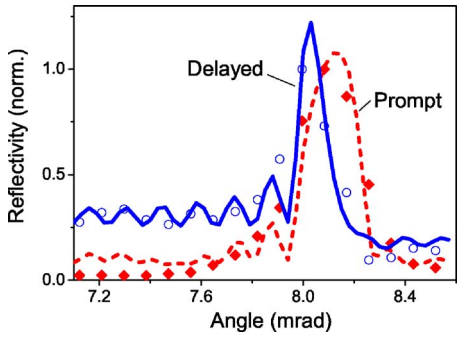

FIG. 16. (Color online) Experimental prompt and delayed first Bragg peaks for the $Si/[Mo/Si]_{45}/^{57}Fe/Nb(70\text{ nm})$ sample. Symbols are the experimental values, solid and dashed lines are the theoretical fits. By the fit of both reflectivity curves we get the exact position $z=5.6$ and thickness $d=3.4$ nm of the ^{57}Fe layer.

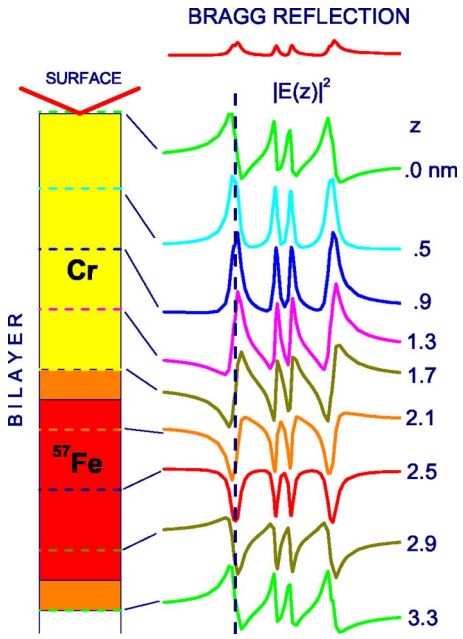

FIG. 17. (Color online) Variations of the energy spectrum of the squared modulus of the total radiation field (energy standing waves) at different depths z (with a 0.4 nm step) inside one bilayer in the periodic structure $[^{57}\mathrm{Fe/Cr}]_{26}$. On the top, the reflectivity spectrum at the exact Bragg is presented in the same energy scale.

case. The standing waves now become energy dependent. If $\chi_i(\omega)$ is described by Eq. (6) it means that the amplitude and the phase of the scattered wave (and reflectivity) drastically changes in the vicinity of each resonant line. According to Eq. (55) the positions of the nodes and antinodes depend on the energy shift in the vicinity of the resonance. At each depth the different spectral frequencies will be enhanced or suppressed. So the resonant standing-wave amplitude changes the shape of its energy spectrum with depth—periodically in the periodic multilayer (Fig. 17). If we follow the variations of the field amplitude with depth for a chosen energy, e.g., at the exact resonance, we get the standing-wave picture presented in Fig. 18. Notice that the positions of the antinodes of the electronic standing wave relative to the periodic structure are different, because the phases of the waves scattered by electronic shells and by resonant nuclei are different at the exact resonance.

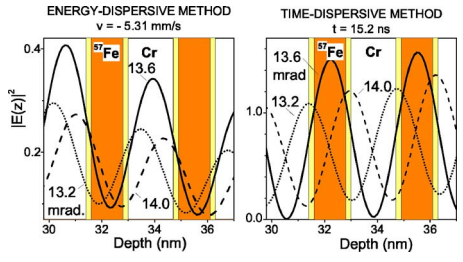

FIG. 18. (Color online) Positions of the nodes and antinodes with respect to the periodic structure at the exact Bragg angle (13.6 mrad) and at the shifted angular positions (13.2 and 14.0 mrad) for the two domains of nuclear resonance excitation. Calculations are made at the exact resonance ($v=-5.31$ mm/s) and at an initial part of the time decay ($t=15.2$ ns).

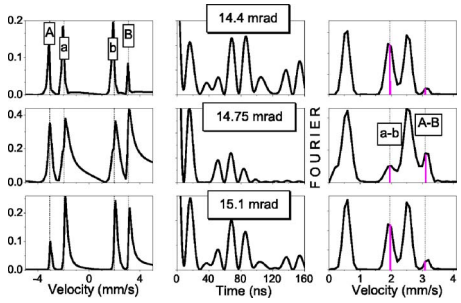

FIG. 19. (Color online) Energy and time spectra of the reflectivity, calculated for three angles in vicinity of the first-order Bragg peak (14.75 mrad). Calculations were done for the periodic multilayer $[^{57}\mathrm{Fe}_{21\mathrm{T}}(0.3\ \mathrm{nm})/^{57}\mathrm{Fe}_{33\mathrm{T}}(0.3\ \mathrm{nm})/^{57}\mathrm{Fe}_{21\mathrm{T}}(0.3\ \mathrm{nm})/\mathrm{V}(2.1\ \mathrm{nm})]_{30}$.

Figure 18 shows also that a slight variation of the angle gives a shift of the standing-wave position, which explains (at least qualitatively) the additional depth selectivity present in the reflectivity spectrum due to the radiation field modulations inside a multilayer. Remembering that the positions of the standing-wave antinodes are different for different frequencies in the spectrum, the variations of the reflectivity spectrum expected from an angle shift are more complicated than the concept of just a pure "scan" across bilayer depth. Anyhow, the calculated example in Fig. 19 demonstrates that we enhance or suppress different spectrum contributions regarding their depth position by the simple angle variation in the vicinity of the Bragg angle, which can be explained by the standing-wave influence on the reflectivity spectrum.

Periodic modulations of the radiation field in the time representation inside a periodic mulilayer have a more complicated nature. Standing waves are the result of the interference of two waves traveling in opposite directions. In the simplest kinematical approximation, however, the incident wave is not changed during propagation in the multilayer and the wave transmitted in the forward direction has no energy dependence. Hence, it is absent in the delayed time representation and a standing wave, which needs two coherently added waves, does not exist.

However, exact calculations show a periodic variation of the field amplitude inside a periodic resonant multilayer also at delayed times (Fig. 18, right side). Moreover, the amplitude of the modulations is enhanced with the depth.[42] Obviously, this is an effect of the transmitted wave modulation; this wave becomes energy dependent during propagation in the resonant multilayer. That explains the enhancement of the standing-wave amplitude with depth.

The difference of the standing-wave pattern in the energy and time representations is very interesting but if we want to have information on the influence of the standing wave in the contributions from a definite layer at some depth z to the reflectivity, we should rely on the general expression (49). In the energy representation the standing-wave picture gives some impression of how different contributions in the spectrum could be enhanced or suppressed. For the time representation we should make a Fourier transform of (49) resulting in the convolution of the separate factors in the product [and in particular the standing-wave factor $(1+R)$]. The in-

fluence of the radiation field structure on the reflectivity becomes more complicated.

The necessity to use the *squared* radiation field amplitude for description of the reflectivity from a thin layer also leads to some new features. The expression $[1+R(\omega)e^{iQH}]$ as such does not give a standing-wave picture in the time representation because the incident wave (normalized to 1) for the phase variation disappears after Fourier transformation, but the squared radiation field (48)

$$[1+R(\omega)e^{iQH}]^2=[1+2R(\omega)e^{iQH}+R^2(\omega)e^{2iQH}] \quad (56)$$

gives the interference of waves with phase difference e^{iQH}, after a Fourier transform, such as

$$2R(t)+R^2(t)e^{iQH}. \quad (57)$$

The effect becomes essential when we cannot neglect the R^2 term in Eq. (56).

After multiplying Eq. (56) by $T(z)T'(z)$, as determined by Eq. (50) or (51), the first term (=1) also contributes to the time dependence of the "effective" radiation field, which has influence on the reflectivity from a layer at depth z. In total, we see that the consideration of this influence on the basis of the standing-wave concept in the time representation becomes equally complicated as that with the Laue function. In that picture we also have an enhancement or suppression of particular frequencies in the resonant spectrum caused by the phase properties of the wave transmission inside the resonant multilayer. In previous papers[42–44] we called this effect a resonant modulation of the radiation field, but its influence on the reflectivity was not fully understood then.

Finally we can conclude that the physics of the nuclear resonant reflectivity becomes very complicated in the general kinematical approximation. Anyhow, when the Bragg reflectivity is relatively high and resonant absorption and refraction effects modify the propagating wave inside a multilayer, not only interference phases but also the resonant excitation conditions for different sublayers are changed with the angle variation. This opens additional possibilities for a determination of the depth distribution of the hyperfine fields by comparing the spectra measured at different angles.

XI. EXPERIMENTAL APPLICATIONS: RESULTS BASED ON THE GENERAL KINEMATICAL APPROXIMATION

The influence of the radiation field structure was taken into account in a depth-selective investigation of monocrystalline periodic multilayers MgO(001)/$[^{57}$Fe(10 ML)/V(5 ML)$]_{20}$/V(5 ML) and MgO(001)/$[^{57}$Fe(7 ML)/V(10 ML)$]_{29}$/Pd(5 ML), denoted $[Fe_{10}/V_5]_{20}$ and $[Fe_7/V_{10}]_{29}$, respectively.[55]

The first-order superstructure Bragg peak for these samples was relatively high. The time spectra of the reflectivity were measured at three angles in the vicinity of the Bragg peak. In such a way we may perform a bilayer depth scan as discussed in previous sections. Anyhow three different spectra, measured at different excitation conditions for the resonant nuclei, give more reliable results than just one spectrum. The results for the sample $[Fe_7/V_{10}]_{29}$ are shown in Fig. 20. The starting model of the hyperfine field parameters for the interpretation of the time spectra was taken from the measured CEMS spectrum which shows a broad hyperfine field distribution [Fig. 20(c)], fitted by six sextets with various Lorentzian linewidths. These hyperfine field parameters and the fractions of each field were then used in the analyses of the reflectivity time spectra [Fig. 20(b)]. Here the purpose of the reflectivity time spectrum fit was only the depth distribution of the known hyperfine fields across one repetition period. We again emphasize that this is the main purpose of the reflectivity spectroscopy. The depth distributions within one repetition period (Fe/V bilayer) of each sextet were simultaneously fitted to the three time spectra. A strongly asymmetrical distribution is found with a noticeable interface intermixing or roughness, in particular at the Fe-on-V interface.

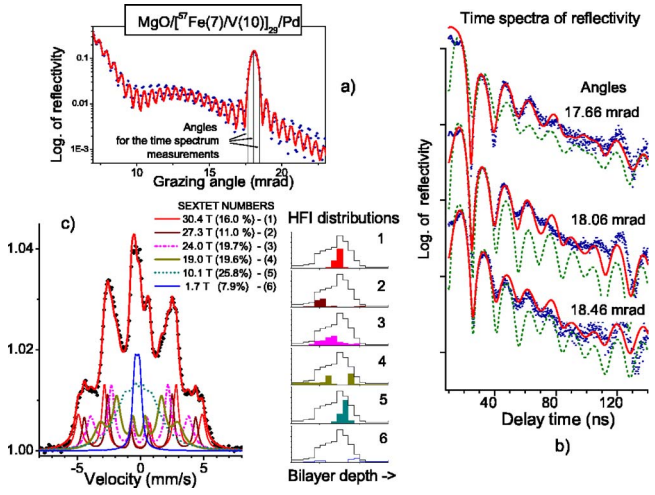

FIG. 20. (Color online) Experimental data for the sample $[^{57}$Fe(7 ML)/V(10 ML)$]_{29}$. (a) Reflectivity. (b) Time spectra of reflectivity for the three angles marked by the vertical lines in (a). (c) CEMS data and the bilayer depth distribution of the different hyperfine field components across one bilayer, as obtained from the fit of the time spectra in (b). The full line in the distribution shows the total ^{57}Fe density. In all graphs dots show experimental data and the full lines the theoretical fits. The dashed curves in (b), not fitting the data, show the expected time spectra assuming a spatially symmetric field distribution in the Fe layers.

The main problem in the reflectivity spectra analysis is a large amount of parameters; namely, the depth distribution of M hyperfine fields in N sublayers is described by $M\times N$ parameters, so the fit of the experimental spectra is most probably not unique. In addition, it relies on the equivalence of all repetition periods in the multilayer which can be infringed at least for the upper or bottom layers due to their interaction with the air or substrate. Additional measurements at higher-order Bragg peaks would make the conclusions more reliable since at these angles the sensitivity to the interface region is stronger. Any peculiarity of the top-layer structure may be revealed by the simultaneous fit of the

reflectivity time spectrum measured near the critical angle of total reflection (as was done in Ref. 41).

XII. ANISOTROPY OF SCATTERING AND POLARIZATION EFFECTS

An essential feature of the nuclear resonant scattering is the anisotropy of the scattering and the specific polarization of each hyperfine transition. If a magnetic hyperfine field $\mathbf{B}_{\mathrm{hf}}$ splits the resonant 14.4 keV transition in ^{57}Fe into six lines, then each hyperfine transition is characterized by a definite state of polarization for the absorbed and reemitted γ quantum depending on the angle of propagation. The angular and polarization dependencies of the nuclear resonant scattering amplitude for separate hyperfine transitions are well known and the appropriate expression through a rotation matrix D was presented just after the discovery of the Mössbauer effect.[65] The perfect formalism describing the transformation of the polarization during propagation in anisotropic Mössbauer medium was presented in the famous paper by Blume and Kistner,[66] who used the two-component vector of the electrical field of radiation (Jones vector) and the 2×2 matrix exponentials as the propagation matrices. Recently this formalism was used for the description of the nuclear resonant forward scattering in the time representation.[67]

For the exact calculations of the reflectivity we use 4×4 propagation matrices taking into account all polarization effects during the multiple scattering in an anisotropic multilayer,[15,35,36,46,47] equivalent to Ref. 68. So far we have used the scalar scattering amplitudes (6) in our kinematical approximation. It is correct only when all scattering amplitudes have one and the same polarization. So our previous consideration was good for samples where all layers are magnetized in one direction and all different kinds of hyperfine transitions do not interfere (the polarization depends on the change of magnetic quantum number $M=m_e-m_g$ in the hyperfine transition between nuclear sublevels, characterized by m_e and m_g in the excited and ground states, respectively). In the energy representation the last requirement is satisfied for well-resolved spectral lines, but in the time representation it implies that all excited transitions should have the same polarization of the scattered radiation. In addition, from the previous consideration we remember that the interference of the nuclear resonant scattering with the electronic scattering plays an essential role in the reflectivity (contrary to the forward scattering where the electronic scattering does not influence the time spectra). The polarization of the electronically scattered radiation is the same as the incident one since in grazing geometry we may neglect the difference in scattering amplitudes for σ- and π- incident polarizations and any polarization can be chosen as an eigenpolarization. Polarization of the nuclear scattering amplitude is determined by the kind of hyperfine transition and the orientation of the incident or scattered radiation relative to the hyperfine field $\mathbf{B}_{\mathrm{hf}}$. Summarizing all circumstances we conclude that the previously presented "scalar" approximation is applicable only to the rather restricted cases, namely, when all layers are magnetized perpendicular to the surface or in the surface but perpendicular to the propagation direction of the radiation. For all other cases the interference of waves of different polarizations appears in some ways. So for completeness it is necessary to include the polarization dependencies of the scattering amplitudes to our structure and Laue factors (15), (16), and (21) or (36) and (37).

We shall follow the Jones vector formalism[66,67] and represent the electric field amplitude of the incident and reflected waves as a column vector. Notice that because the angular dependencies of the amplitude and polarization of the hyperfine transitions are rather smooth, we can suppose (just for the polarization description) that both waves propagate along the surface in grazing geometry. (It works even in the general dynamical approximation.[47]) Then the bases for the description of the polarization of both waves are the same, horizontal (x axis) and vertical (z axis) with the direction of the wave propagation along the y axis,

$$\mathbf{E}=\begin{pmatrix}E_x\\E_z\end{pmatrix}. \tag{58}$$

Then the polarization of the incident synchrotron radiation is presented by the vector $\binom{1}{0}$. The nuclear resonant scattering amplitude is transformed to the 2×2 matrix

$$\hat{f}^{\,\mathrm{nuc}}(\omega)=-\frac{1}{2\lambda}\sigma_{\mathrm{res}}f^{\,\mathrm{LM}}P\sum_i\frac{\hat{\alpha}_i\Gamma_i/2\hbar}{\omega-\omega_i+i\Gamma_i/2\hbar}. \tag{59}$$

The explicit form of the polarization 2×2 matrices $\hat{\alpha}_i$ for each hyperfine transition is determined by the multipolarity of the transition and by the spins of the ground and excited nuclear states. For each of the six hyperfine lines in the magnetic spectrum in the case of the magnetic dipole $M1$ transition between levels $I_g=1/2$, $I_e=3/2$ (as in ^{57}Fe) we have

$$\hat{\alpha}_1=\frac{3}{8}\begin{pmatrix}\sin^2\beta & \sin\beta(\cos\beta\cos\gamma-i\sin\gamma)\\ \sin\beta(\cos\beta\cos\gamma+i\sin\gamma) & \cos^2\beta\cos^2\gamma+\sin^2\gamma\end{pmatrix},$$

$$\hat{\alpha}_2=\frac{1}{2}\begin{pmatrix}\cos^2\beta & -\sin\beta\cos\beta\cos\gamma\\ -\sin\beta\cos\beta\cos\gamma & \sin^2\beta\cos^2\gamma\end{pmatrix},$$

$$\hat{\alpha}_3=\frac{1}{3}\hat{\alpha}_1^*,\quad \hat{\alpha}_4=\frac{1}{3}\hat{\alpha}_1,\quad \hat{\alpha}_5=\hat{\alpha}_2,\quad \hat{\alpha}_6=\hat{\alpha}_1^*, \tag{60}$$

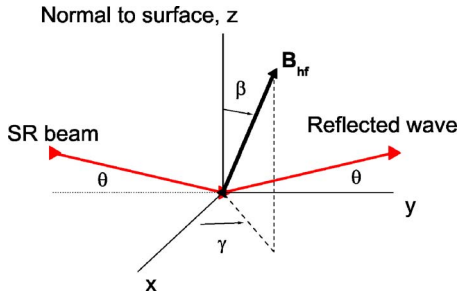

FIG. 21. (Color online) Angles for determination of the $\mathbf{B}_{\mathrm{hf}}$ orientation relative to the reflectivity geometry.

the orientation of the magnetic hyperfine field being determined by the polar angle β and the azimuthal angle γ in the chosen frame of axes (Fig. 21). We should add also that the electronic scattering amplitude now is transformed to a diagonal matrix.

With $\hat{f}^{\mathrm{nuc}}(\omega)$ determined by Eq. (59) the structure factor (21) also becomes a matrix, which determines in particular the polarization of the scattered wave by one repetition period in the simplest kinematical approximation. From Eq. (60) it follows that for $\beta=0$ only the second and fifth resonant lines appear in the reflectivity spectrum, and the polarization of the scattered radiation is the same as the polarization of the incident synchrotron radiation (this case was considered in our model calculations). For $\beta=90°$, $\gamma=0$ the second and fifth resonant lines are not excited at all and the other four lines have the same polarization as the incident SR beam. For $\beta=90°$, $\gamma=90°$ the polarization of the first and fourth scattered lines is right circular $\left[\sim\binom{1}{i}\right]$ and the polarization of the third and sixth lines is left circular $\left[\sim\binom{1}{-i}\right]$, which means that the interference term will appear only for each pair of lines. The corresponding time spectrum of reflectivity will have just one beat frequency (Fig. 22). These specific cases were considered for the forward scattering.[21,67] In Ref. 67 a nice illustration of the rotation of the resulting linear polarization, with a beat frequency corresponding to the frequency difference of the right and left circular scattered polarizations, was presented for the last case ($\beta=90°, \gamma=90°$). Interference of the waves with orthogonal polarization does not give any interference term in the resulting intensity, but leads to a variation of the polarization state. For other angles all lines should be taken into account. So the number of beat frequencies in the time spectrum of reflectivity indeed characterizes the orientation of the hyperfine field in the investigated multilayer (some restrictions follow from indistinguishable situations presented also in Fig. 22).

With the help of Eqs. (59), (60), and (21) we can analyze how the depth variation of the hyperfine field orientation will reveal itself in the time spectrum of reflectivity. For example, we can compare the two cases: when antiferromagnetic alignment takes place within one sublayer or when two sublayers separated by depth distance d are antiferromagnetically coupled. Supposing $\beta=90°$, $\gamma=90°$, and omitting some trivial factors and the exponential decay factor $e[-(\Gamma/2\hbar)t]$, we obtain for the single-nucleus scattering amplitude in Eq. (21) in the time representation

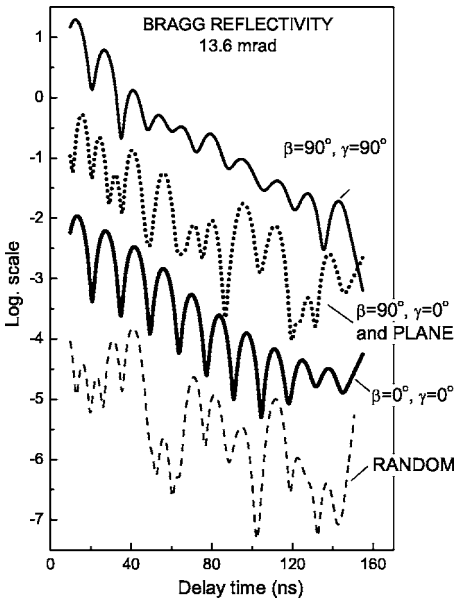

FIG. 22. Time spectra of reflectivity from the resonant multilayer $[^{57}\mathrm{Fe/Cr}]_{26}$ calculated for the exact Bragg angle with different directions and types of magnetic alignment.

$$f_1(t) \propto e^{i\omega_1 t}\begin{pmatrix}1\\ i\end{pmatrix} + e^{i\omega_3 t}\frac{1}{3}\begin{pmatrix}1\\ -i\end{pmatrix} + e^{i\omega_4 t}\frac{1}{3}\begin{pmatrix}1\\ i\end{pmatrix} + e^{i\omega_6 t}\begin{pmatrix}1\\ -i\end{pmatrix} \tag{61}$$

since only four resonant transitions (1,3,4,6) are excited by the σ-polarized incident radiation. If a second resonant layer in one repetition period is characterized by $-\mathbf{B}_{\mathrm{hf}}$ ($\beta=90°, \gamma=-90°$) then

$$f_2(t) \propto e^{i\omega_1 t}\begin{pmatrix}1\\ -i\end{pmatrix} + e^{i\omega_3 t}\frac{1}{3}\begin{pmatrix}1\\ i\end{pmatrix} + e^{i\omega_4 t}\frac{1}{3}\begin{pmatrix}1\\ -i\end{pmatrix} + e^{i\omega_6 t}\begin{pmatrix}1\\ i\end{pmatrix}. \tag{62}$$

Constructing the structure factor (21) we should add Eqs. (61) and (62) with the appropriate space phase shift Δ according to Eq. (31). If $\Delta=0$, as for an antiferromagnetic alignment within one sublayer, then all frequencies in the scattered radiation are linear σ polarized and we have multifrequency beats in the time spectrum (see Fig. 23).

For $\Delta=\pi$ all components in the scattered radiation are again linear polarized, but along the z direction, the spectrum of reflectivity being the same. But if $\Delta=\pi/2$ we obtain

$$F(t) \propto (1+i)\left[e^{i\omega_1 t}\begin{pmatrix}1\\ 1\end{pmatrix} + e^{i\omega_3 t}\frac{1}{3}\begin{pmatrix}1\\ -1\end{pmatrix} + e^{i\omega_4 t}\frac{1}{3}\begin{pmatrix}1\\ 1\end{pmatrix} + e^{i\omega_6 t}\begin{pmatrix}1\\ -1\end{pmatrix}\right] \tag{63}$$

so the first and fourth lines have a linear polarization rotated by 45° relative to the x,z axes (see Fig. 24), and the third and sixth components are also linearly polarized but orthogonal to the linear polarization of the first and fourth lines. The time spectrum of reflectivity will have a single quantum beat frequency (Fig. 23). This is a clear example of how the space

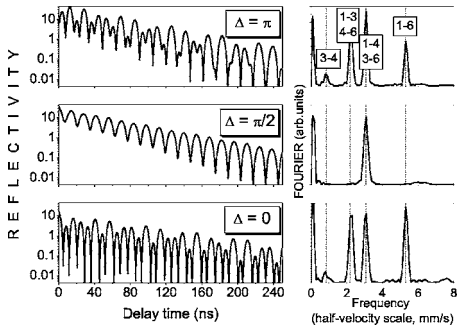

FIG. 23. Time spectra of the Bragg reflectivity (left) and their Fourier transforms (right) calculated for the multilayer $[V/^{57}Fe/^{56}Fe/^{57}Fe]_{30}$ with the two antiferromagnetically ordered ($\mathbf{B}_{hf}$ along the beam) resonant ^{57}Fe sublayers at different positions in the repetition period: $\Delta=\pi$ (top), $\pi/2$ (middle), and 0 (bottom).

phase shift can change not only the phase or intensity of different contributions but also the state of polarization. The structure information will in this situation be even richer (especially if we select the polarization state of the reflectivity).

For the general kinematical approximation the transformation of the polarization state of the radiation, during its propagation through the sample, should be considered in addition to the refraction and absorption corrections and the formula (11) should be generalized to

$$\hat{R}=\frac{1}{4\sin^2\vartheta}\sum_{j=1}^{L} e^{iQz_{j-1}}e^{(\kappa/\sin\vartheta)\hat{\chi}_{\perp_1}d_1}e^{(\kappa/\sin\vartheta)\hat{\chi}_{\perp_2}d_2}\cdots \times e^{(\kappa/\sin\vartheta)\hat{\chi}_{\perp_{j-1}}d_{j-1}}(\hat{\chi}_{\perp_{j-1}}-\hat{\chi}_{\perp_j}) \times e^{(\kappa/\sin\vartheta)\hat{\chi}_{\perp_{j-1}}d_{j-1}}\cdots e^{(\kappa/\sin\vartheta)\hat{\chi}_{\perp_2}d_2}e^{(\kappa/\sin\vartheta)\hat{\chi}_{\perp_1}d_1}. \quad (64)$$

Here the reflectivity is calculated as a sum of the reflectivities at each jth boundary in a multilayer with the additional (to the simplest $e^{iQz_{j-1}}$) phase shift, absorption, and polarization transformation determined by the matrix exponentials $e^{(\kappa/\sin\vartheta)\hat{\chi}_{\perp n}d_n}$, sequentially in all layers above the jth layer: $n=1,2,\ldots j-1$. If the structure contains several kinds of hyperfine fields and the structure factor does not commute with the 2×2 propagation matrices $e^{\pm i\hat{\eta}\kappa z}$ then factorization of

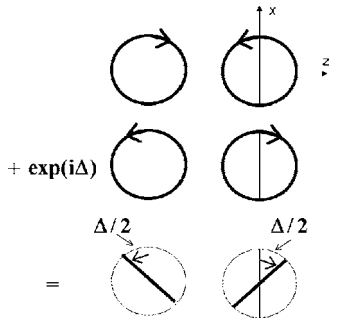

FIG. 24. Addition of the right and left or left and right circular polarizations with the space shift $\boldsymbol{\Delta}$. If $\boldsymbol{\Delta}=\boldsymbol{\pi}/2$ the resulting linear polarizations are orthogonal.

Eq. (57), as of Eq. (17), is unfortunately impossible. At that point any qualitative description of the reflectivity process is practically impossible. We can only add that exactly as it occurs for the resonant dependence of the reflectivity, the polarization transformation of the waves with depth implies that the electronic charge scattering will participate in the creation of a polarization state of the reflected radiation different from the incident one.

The kinematical approach gives us anyway only a qualitative picture of the interaction. So finally we present here the correct dynamical formula of reflectivity which we have used in our fit programs of the reflectivity. It is a generalization of the Parratt recurent algorithm[45] for the case when the transformation of polarization states of radiation should be taken into account:

$$\hat{R}_j=\hat{r}_j+\hat{t}'_j(1-\hat{R}^{up}_{j+1}\hat{r}'_j)^{-1}\hat{R}^{up}_{j+1}\hat{t}_j, \quad (65)$$

where

$$\hat{R}^{up}_{j+1}=e^{-i\hat{\eta}^-_j\kappa d_j}\hat{R}_{j+1}e^{i\hat{\eta}^+_j\kappa d_j} \quad (66)$$

and $\hat{r}_j$, $\hat{t}_j$, $\hat{r}'_j$, and $\hat{t}'_j$ are the 2×2 matrices (planar tensors) of the reflection and transmission for the boundary between sublayers $j-1$ and j and the prime indicates the propagation in the backward direction, and $\hat{\eta}^{\pm}_j$ are the tensors of the normal refraction for the waves in the forward and backward directions.[46] Notice in conclusion that the calculations by this formula give exactly the same result as calculations with the 4×4 propagation matrix method.[47,68]

XIII. EXPERIMENTAL APPLICATION: $[Fe/Cr]_{26}$

The time spectra of reflectivity, measured for the sample glass/Cr(50)/$[^{57}Fe(1.7)/Cr(1.6)]_{26}$/Zr(10) (nominal thickness in nanometers), having a rather high reflectivity at the first Bragg peak, can be a good illustration of the influence of the standing waves and polarization mixing on the reflectivity spectra.[62–64] The time spectra were measured for several angles in vicinity of the Bragg angle (13.2, 13.6, 13.8, and 14.0 mrad) at room temperature without external magnetic field (Fig. 25). It was clearly seen (and confirmed by the Fourier analysis) that the time spectra measured with a very small change of the incident angle (0.2 mrad) are rather different.

The most surprising thing was the appearance of new beat frequencies at angles slightly different from the exact Bragg angle. We supposed that the contribution from the middle part of the ^{57}Fe layer is enhanced in the time spectra measured at the exact Bragg angle 13.58 mrad while the time spectra measured with some shift from the exact Bragg angle characterize mostly the interface regions. The depth distribution of the magnitude and orientation of the hyperfine fields $\mathbf{B}_{hf,i}(z)$ on the scale of one bilayer was obtained by a fit of the experimental time spectra (Fig. 26).

For the description of the orientation of the hyperfine field $\mathbf{B}_{hf}$ in each sublayer three states were used. They were (i) definite values of polar β and azimuth γ angles for $\mathbf{B}_{hf}$, (ii) "random," which means random in 4π solid angle, and (iii) "in plane," a random distribution of $\mathbf{B}_{hf}$ in the surface plane.

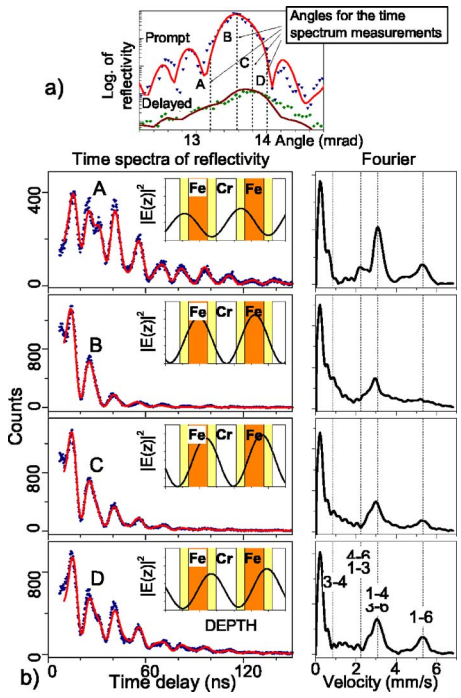

FIG. 25. (Color online) Prompt and delayed reflectivity for 0.086 nm SR near the Bragg peak (top) and the experimental time spectra (left) with their Fourier transforms (right) for four angles in the vicinity of the Bragg peak (marked by vertical dashed lines). Insets show the standing-wave pattern for the chosen angles calculated at the delay time 11.8 ns. Vertical dotted lines across the Fourier spectra show the quantum beat frequencies corresponding to the interference between the Mössbauer lines in α-iron, numbered in the bottom panel. Theoretical (solid) curves are the result of the fit. The obtained model for the spatial field distribution is shown in Fig. 26.

Notice that the in-plane state is ambiguous since several other orientations of $\mathbf{B}_{\mathrm{hf}}$ give exactly the same time spectrum. They are (1) an antiferromagnetic ordering of the magnetic moments (or domains) along any direction in the surface plane and (2) a perpendicular orientation of $\mathbf{B}_{\mathrm{hf}}$ to the radiation beam but still in the surface plane. The best fit was obtained with $\mathbf{B}_{\mathrm{hf},i}$ in the middle part of ^{57}Fe layers lying in the surface plane at an angle $\cong 40°$ with the direction of the beam, but with some fraction of the $\mathbf{B}_{\mathrm{hf},i}$ in the interface regions having random orientation in the plane ($\sim 40\%$) and even in space ($\sim 20\%$). Hence, we revealed the noncollinear magnetic ordering in our multilayer.

As it could be expected the smaller value of $\mathbf{B}_{\mathrm{hf}}$ was detected to be preferably situated in the interface regions of the ^{57}Fe/Cr bilayer (Fig. 26). We clearly observed also an asymmetry of the Fe-on-Cr and Cr-on-Fe interfaces characterized by the thickness of the Fe-on-Cr interface ~ 1 nm, but the Cr-on-Fe interface by only ~ 0.2 nm. That evidenced that the roughness of the chromium surfaces is larger than that of the iron surfaces in our structure. Remember that the investigations of the difference of the interfaces by means of one ^{57}Fe probe monolayer (see, e.g., Refs. 3 and 4) are rather ambiguous because it is practically impossible to prepare two identical samples with ^{57}Fe at different interfaces or layers (unless wedged samples are produced). By means of the standing waves we may investigate both interfaces in one and the same sample.

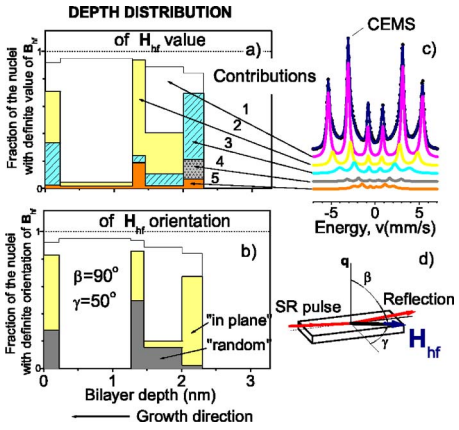

FIG. 26. (Color online) The obtained depth distribution of the $\mathbf{B}_{\mathrm{hf}}$ values (a) and $\mathbf{B}_{\mathrm{hf}}$ orientations (b) in one ^{57}Fe/Cr bilayer. Horizontal dotted lines in (a) and (b) are the normalization values; corresponding to the density of pure α-iron. The normal CEMS spectrum and its fit is shown in (c). (d) shows the angles β and γ and the obtained preferred magnetic moment orientation in our ^{57}Fe/Cr superstructure.

XIV. INTERFACE AND LAYER INHOMOGENEITIES AND THE REFLECTIVITY SPECTRUM

In previous sections we have discussed the influence of the depth distribution of the hyperfine fields on the reflectivity spectrum. Real samples, however, are usually not uniform along the interfaces. Initial stages of film growth are often characterized by island formation, monocrystalline films have steps, terraces, and so on. Such inhomogeneities are always characterized by specific hyperfine fields (that is why the Mössbauer spectra of thin films and even monolayers have such a complicated spectral content). It is well known that the surface and interface roughness as well as the volume inhomogeneities (such as magnetic domains) create a diffuse scattering and decrease the specular reflectivity. Such influence on the reflectivity can be described by Debye or Nevot-Croce damping factors or by introducing an interface layer with a density gradient between the sublayers. Such a description is good in the ordinary x-ray reflectivity, but it is not sufficient for the coherent reflection spectroscopy.

If we are interested in the different resonant contributions to the reflectivity spectrum we should realize that one and the same amount of a given hyperfine contribution will be present in the reflectivity spectrum with different weights depending on the degree of the distribution smoothness of the corresponding nuclei along the layer plane.

Figure 27 illustrates this idea. If resonant nuclei are collected in small irregular grains (with zero correlation length), then their contribution to the coherent reflectivity signal will be negligible [Fig. 27(b)]. The contributions from "island regions" at the interfaces will be more essential [Fig. 27(c)] but smaller than those from from the uniform layers [Fig. 27(a)].

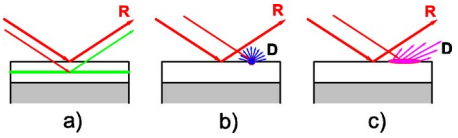

FIG. 27. (Color online) Illustration of the difference in the hyperfine spectrum contributions to the reflectivity spectrum originating from the nonuniform interface distribution of the scattering nuclei.

In addition, we should remember that the size of the detector slits could substantially change the relative amount of different resonant contributions by measuring some part of the diffuse scattering. The exact theory of such suppression or enhancement of the different hyperfine contributions has not been developed yet, but qualitatively we can interpret the decrease of some hyperfine field fractions, as derived from the reflectivity spectrum compared to a corresponding CEMS spectrum, as due to the nonuniform in-the-layer or interface distribution of these components.

XV. CONCLUSIONS

Coherent nuclear resonance reflectivity spectroscopy differs from the conventional absorption (e.g., Mössbauer) spectroscopy in many aspects and the interpretation of the experimental spectra may be rather intricate. However, one advantage is the sensitivity to the depth distribution of different hyperfine fields and it is an alternative method to the ^{57}Fe probe monolayer method[3,4] for such depth-selective investigations.

The presented analysis of the basic features of the coherent spectroscopy at Bragg reflections from periodic multilayers mainly refers to the nuclear resonant scattering of SR. However, the here revealed peculiarities in the energy representation are general properties of the reflectivity process and may also be applied to the data interpretation of any kind of reflectivity spectroscopy, in particular for resonant x-ray scattering.

ACKNOWLEDGMENTS

The work was supported by RFBR (Grants No. 01-02-17541, No. 03-02-17168, and No. 05-02-16770), by INTAS (Grant No. 01-0822), and by the Royal Swedish Academy of Sciences. The authors are thankful to their colleagues for the sample preparations and their characterizations and to the ESRF staff for the great assistance with nuclear resonant reflectivity measurements.

[1] J. B. Kortright, D. D. Awschalom, J. Stöhr, S. D. Bader, Y. U. Idzerda, S. S. P. Parkin, I. K. Schuller, and H.-C. Siegmann, J. Magn. Magn. Mater. **207**, 7 (1999).
[2] P. Panissod, J. P. Jay, C. Meny, M. Wojcik, and E. Jedryka, Hyperfine Interact. **97/98**, 75 (1996).
[3] B. Kalska, P. Blomquist, L. Häggström, and R. Wäppling, Europhys. Lett. **53**, 395 (2001).
[4] T. Shinjo and W. Keune, J. Magn. Magn. Mater. **200**, 598 (1999).
[5] L. Niesen, A. Mugarza, M. F. Rosu, R. Coehoorn, R. M. Jungblut, F. Roozeboom, A. Q. R. Baron, A. I. Chumakov, and R. Rüffer, Phys. Rev. B **58**, 8590 (1998).
[6] R. Röhlsberger, H. Thomas, K. Schlage, E. Burkel, O. Leupold, and R. Rüffer, Phys. Rev. Lett. **89**, 237201 (2002).
[7] C. Carbone, A. Dallmeyer, M. C. Malagoli, K. Maiti, J. Wingbermühle, W. Eberhardt, D. L. Nagy, L. Bottyán, L. Deák, E. Szilágy, and R. Rüffer, ESRF Highlights , p. 60 (1999).
[8] S. Bernstein and E. C. Campbell, Phys. Rev. **132**, 1625 (1963).
[9] F. E. Wagner, Z. Phys. **210**, 361 (1968).
[10] J. C. Frost, B. C. C. Cowie, S. N. Chapman, and J. P. Marshall, Appl. Phys. Lett. **47**, 581 (1985).
[11] M. A. Andreeva, G. N. Belozerskii, S. M. Irkaev, V. G. Semenov, A. Yu. Sokolov, and N. V. Shumilova, Phys. Status Solidi A **127**, 455 (1991).
[12] A. I. Chumakov, G. V. Smirnov, S. S. Andreev, N. N. Salashchenko, and S. I. Shinkarev, JETP Lett. **55**, 509 (1992).
[13] R. Röhlsberger, E. Witthoff, E. Gerdau, and E. Lüken, J. Appl. Phys. **74**, 1933 (1993).
[14] R. Röhlsberger, E. Gerdau, E. Lüken, H. D. Rüter, J. Metge, and O. Leupold, Z. Phys. B: Condens. Matter **92**, 489 (1993).
[15] S. M. Irkaev, M. A. Andreeva, G. N. Belozerskii, V. G. Semenov, and O. V. Grishin, Nucl. Instrum. Methods Phys. Res. B **74**, 545 (1993); **74**, 554 (1993); **103**, 351 (1995).
[16] S. A. Isaenko, A. I. Chumakov, and S. I. Shinkarev, Phys. Lett. A **186**, 274 (1994).
[17] M. A. Andreeva, S. M. Irkaev, D. O. Neplokhov, N. N. Polushkin, N. N. Salashchenko, and V. G. Semenov, Surf. Invest. X-Ray Synchrotron Neutron Tech. **13**, 1529 (1998).
[18] *Mössbauer Spectroscopy II: The Exotic Side of the Method*, edited by U. Gonser (Springer-Verlag, Berlin, 1981), Chap. 3.3.
[19] A. I. Chumakov, L. Niesen, D. L. Nagy, and E. E. Alp, Hyperfine Interact. **123/124**, 427 (1999).
[20] R. Rüffer and A. I. Chumakov, Hyperfine Interact. **97/98**, 589 (1996).
[21] V. G. Smirnov, Hyperfine Interact. **123/124**, 31 (1999).
[22] T. S. Toellner, W. Sturhahn, R. Röhlsberger, E. E. Alp, C. H. Sowers, and E. E. Fullerton, Phys. Rev. Lett. **74**, 3475 (1995).
[23] A. Q. R. Baron, J. Arthur, S. L. Ruby, A. I. Chumakov, G. V. Smirnov, and G. S. Brown, Phys. Rev. B **50**, 10354 (1994).
[24] L. Bottyán, J. Dekoster, L. Deák, A. Q. R. Baron, S. Degroote, R. Moons, D. L. Nagy, and G. Langouche, Hyperfine Interact. **113**, 295 (1998).
[25] M. A. Andreeva and B. Lindgren, JETP Lett. **76**, 704 (2002).
[26] L. Nevot and P. Croce, Rev. Phys. Appl. **15**, 761 (1980).
[27] D. K. G. de Boer, Phys. Rev. B **49**, 5817 (1994).
[28] J. P. Hannon, G. T. Trammell, M. Mueller, E. Gerdau, H. Winkler, and R. Rüffer, Phys. Rev. Lett. **43**, 636 (1979).
[29] J. P. Hannon, N. V. Hung, G. T. Trammell, E. Gerdau, M. Mueller, R. Rüffer, and H. Winkler, Phys. Rev. B **32**, 5068 (1985); **32**, 5081 (1985).
[30] J. P. Hannon, G. T. Trammell, M. Mueller, E. Gerdau, R. Rüffer,

and H. Winkler, Phys. Rev. B **32**, 6363 (1985); **32**, 6374 (1985).
[31] R. Röhlsberger, Hyperfine Interact. **123/124**, 455 (1999).
[32] M. A. Andreeva, JETP Lett. **68**, 480 (1998).
[33] M. A. Andreeva, S. M. Irkaev, K. A. Prokhorov, N. N. Salashchenko, V. G. Semenov, A. I. Chumakov, and R. Rüffer, Surf. Invest. X-Ray Synchrotron Neutron Tech. **15**, 83 (1999).
[34] M. A. Andreeva, G. N. Belozerskii, O. V. Grishin, S. M. Irkaev, V. I. Nikolaev, and V. G. Semenov, JETP Lett. **55**, 63 (1992).
[35] M. A. Andreeva, S. M. Irkaev, and V. G. Semenov, JETP **78**, 956 (1994).
[36] M. A. Andreeva, S. M. Irkaev, and V. G. Semenov, Hyperfine Interact. **97/98**, 605 (1996).
[37] A. I. Chumakov, G. V. Smirnov, A. Q. R. Baron, J. Arthur, D. E. Brown, S. L. Ruby, G. S. Brown, and N. N. Salashchenko, Phys. Rev. Lett. **71**, 2489 (1993).
[38] D. L. Nagy, L. Bottyán, L. Deák, J. Dekoster, G. Langouche, V. G. Semenov, H. Spiering, and E. Szilágyi, in *Mössbauer Spectroscopy in Materials Science*, edited by M. Miglierini and D. Petridis (Kluwer Academic, Dordrecht, 1999), p. 323.
[39] L. Sève, N. Jaouen, J. M. Tonnerre, D. Raoux, F. Bartolome, M. Arend, W. Felsch, A. Rogalev, J. Goulon, C. Gautier, and J. F. Bérar, Phys. Rev. B **60**, 9662 (1999).
[40] I. W. Hamley and J. S. Pedersen, J. Appl. Crystallogr. **27**, 29 (1994).
[41] M. A. Andreeva, S. M. Irkaev, V. G. Semenov, K. A. Prokhorov, N. N. Salashchenko, A. I. Chumakov, and R. Rüffer, J. Alloys Compd. **286**, 322 (1999).
[42] M. A. Andreeva, JETP Lett. **69**, 863 (1999).
[43] M. A. Andreeva, S. M. Irkaev, V. G. Semenov, K. A. Prokhorov, N. N. Salashchenko, A. I. Chumakov, and R. Rüffer, Hyperfine Interact. **126**, 343 (2000).
[44] M. A. Andreeva, Surf. Invest. X-Ray Synchrotron Neutron Tech. **16**, 9 (2001).
[45] L. G. Parratt, Phys. Rev. **95**, 359 (1954).
[46] G. N. Borzdov, L. M. Barkovskii, and V. I. Lavrukovich, Zh. Prikl. Spektrosk. **25**, 526 (1976).
[47] M. A. Andreeva and K. Rosete, Vestn. Mosk. Univ., Fiz., Astron. **41**, 65 (1986) [Moscow Univ. Phys. Bull. **41**, 65 (1986)]; Poverkhnost No. 9, 145 (1986).
[48] http://csrri.iit.edu/periodic-table.html/
[49] ftp://xray.uu.se/pub/henke/sf/
[50] www.unca.edu/medc
[51] V. I. Iveronova and G. P. Revkevich, *Theory of X-ray Scattering* (Moscow University Press, Moscow, 1972) (in Russian).
[52] R. James, *Optical Principles of X-ray Diffraction* (Foreign Literary Publications, Moscow, 1950).
[53] B. Lindgren, M. A. Andreeva, L. Häggström, B. Kalska, V. G. Semenov, A. I. Chumakov, O. Leupold, and R. Rüffer, Hyperfine Interact. **136/137**, 439 (2001).
[54] B. Lindgren, M. A. Andreeva, L. Häggström, B. Kalska, O. Leupold, and R. Rüffer, in European Workshop on Nuclear Resonant Scattering for the Study of Nanoscale Structures, ESRF, Grenoble, France 2004 (unpublished).
[55] B. Kalska, L. Häggström, B. Lindgren, P. Blomquist, R. Wäppling, M. A. Andreeva, Yu. V. Nikitenko, V. V. Proglyado, V. L. Aksenov, V. G. Semenov, A. I. Chumakov, O. Leupold, and R. Rüffer, Hyperfine Interact. **136/137**, 295 (2001).
[56] M. V. Koval'chuk and V. G. Kohn, Usp. Fiz. Nauk **149**, 69 (1986).
[57] M. J. Bedzyk, G. M. Bommarito, and J. S. Schildkraut, Phys. Rev. Lett. **62**, 1376 (1989).
[58] M. A. Andreeva, JETP Lett. **62**, 921 (1995).
[59] M. A. Andreeva, Phys. Lett. A **210**, 359 (1996).
[60] M. A. Andreeva, Proc. SPIE **4605**, 368 (2001).
[61] M. A. Andreeva, S. N. Vdovichev, Yu. N. Nozdrin, E. E. Pestov, N. N. Salashchenko, V. G. Semenov, B. Lindgren, L. Häggström, P. Nordblad, B. Kalska, O. Leupold, and R. Rüffer, Izv. Akad. Nauk, Ser. Fiz. **68**, 487 (2004).
[62] M. A. Andreeva, V. G. Semenov, L. Häggström, B. Lindgren, B. Kalska, A. I. Chumakov, O. Leupold, R. Rüffer, K. A. Prokhorov, and N. N. Salashchenko, Phys. Met. Metallogr. **91** Suppl. 1, 22 (2001).
[63] M. A. Andreeva, V. G. Semenov, L. Häggström, B. Kalska, B. Lindgren, A. I. Chumakov, O. Leupold, and R. Rüffer, Hyperfine Interact. **136/137**, 687 (2001).
[64] M. A. Andreeva, V. G. Semenov, B. Lindgren, L. Häggström, B. Kalska, A. I. Chumakov, O. Leupold, R. Rüffer, K. A. Prokhorov, and N. N. Salashchenko, Hyperfine Interact. **141/142**, 119 (2002).
[65] G. T. Trammell, Phys. Rev. **126**, 1045 (1962).
[66] M. Blum and O. C. Kistner, Phys. Rev. **171**, 417 (1968).
[67] D. P. Siddons, U. Bergmann, and J. B. Hastings, Hyperfine Interact. **123/124**, 681 (1999).
[68] R. Röhlsberger, Hyperfine Interact. **123/124**, 301 (1999).